



Aalborg Universitet

AALBORG UNIVERSITY
DENMARK

A Gray-Box Hierarchical Oscillatory Instability Source Identification Method of Multiple-Inverter-Fed Power Systems

Zhou, Weihua; E. Torres-Olguin, Raymundo; Wang, Yanbo; Chen, Zhe

Published in:

I E E E Journal of Emerging and Selected Topics in Power Electronics

DOI (link to publication from Publisher):

[10.1109/JESTPE.2020.2992225](https://doi.org/10.1109/JESTPE.2020.2992225)

Publication date:

2021

Document Version

Accepted author manuscript, peer reviewed version

[Link to publication from Aalborg University](#)

Citation for published version (APA):

Zhou, W., E. Torres-Olguin, R., Wang, Y., & Chen, Z. (2021). A Gray-Box Hierarchical Oscillatory Instability Source Identification Method of Multiple-Inverter-Fed Power Systems. *I E E E Journal of Emerging and Selected Topics in Power Electronics*, 9(3), 3095-3113. Advance online publication. <https://doi.org/10.1109/JESTPE.2020.2992225>

General rights

Copyright and moral rights for the publications made accessible in the public portal are retained by the authors and/or other copyright owners and it is a condition of accessing publications that users recognise and abide by the legal requirements associated with these rights.

- Users may download and print one copy of any publication from the public portal for the purpose of private study or research.
- You may not further distribute the material or use it for any profit-making activity or commercial gain
- You may freely distribute the URL identifying the publication in the public portal -

Take down policy

If you believe that this document breaches copyright please contact us at vbn@aub.aau.dk providing details, and we will remove access to the work immediately and investigate your claim.

A Gray-Box Hierarchical Oscillatory Instability Source Identification Method of Multiple-Inverter-Fed Power Systems

Weihua Zhou, *Student Member, IEEE*, Raymundo E. Torres-Olguin, Yanbo Wang, *Senior Member, IEEE*, and Zhe Chen, *Fellow, IEEE*

Abstract—This paper presents a gray-box hierarchical instability source identification method of multiple-inverter-fed power systems, which enables stability analysis at system, component, and parameter levels sequentially. Impedance frequency responses of all components are first obtained using frequency scanning method. System impedance network model is then established by connecting these individual components based on system topology, which is further lumped into a loop impedance model (LIM). The vector fitting (VF) algorithm is then used to generate system state-space model from the impedance frequency responses of the LIM for eigenvalues-based stability analysis. If the system is assessed to be unstable, problematic components are further identified by performing impedance-based stability criterion at terminals of all components, where the numbers of right-half-plane poles are obtained by the VF algorithm. Finally, circuit and controller parameters of the identified problematic components are further identified using the VF algorithm, which are re-tuned to improve system stability. The proposed hierarchical instability source identification method is implemented in a multiple-paralleled grid-connected inverter system. Simulation results obtained in Matlab/Simulink platform and real-time simulation verification results obtained in OPAL-RT platform are given to validate the correctness of the theoretical analysis results.

Index Terms—Eigenvalues analysis, frequency scanning, grid-connected inverter, impedance-based stability criterion, instability, loop impedance model, vector fitting algorithm.

NOMENCLATURE

Abbreviations

GCI	Grid-connected inverter.
IBSC	Impedance-based stability criterion.
INM	Impedance network model.
LIM	Loop impedance model.
NAM	Nodal admittance matrix.
NC	Nyquist criterion.
NPR	Non-passivity region.
P.u.l.	Per-unit-length.
PCC	Point of common coupling.
PF	Participation factor.

This work was supported by the ForskEL and EUDP project “Voltage Control and Protection for a Grid towards 100% Power Electronics and Cable Network (COPE)” (Project No.: 880063). Portion of this work was presented at the ICPE-ECCE ASIA, Busan, Korea, May 27–30, 2019 [1]. (*Corresponding author: Weihua Zhou*).

W. Zhou, Y. Wang and Z. Chen are with the Department of Energy Technology, Aalborg University, 9220 Aalborg, Denmark (e-mail: wez@et.aau.dk; ywa@et.aau.dk; zch@et.aau.dk).

R. E. Torres-Olguin is with the SINTEF Energy Research Institute, 7034 Trondheim, Norway (e-mail: raymundo.torres-olguin@sintef.no).

PI	Proportional integral.
PLL	Phase-locked loop.
RHP	Right-half-plane.
SSM	State-space model.
VF, MF	Vector fitting and matrix fitting.
<i>Symbols</i>	
ω_1	Grid fundamental angular frequency.
Θ, \oplus	Parallel and series connection operators.
$A_{iL}, B_{iL}, C_{iL}, D_{iL}$	State matrices of load part divided at node $\#i$.
$A_{iS}, B_{iS}, C_{iS}, D_{iS}$	State matrices of source part divided at node $\#i$.
A_{sys}, X_{sys}	Transition matrix and state-variable vector of the whole system.
C_f	Filter capacitance.
f_{sw}, f_s, T_s	Switching frequency, sampling frequency, and sampling time.
$I_{g,d}^{ref}, I_{g,q}^{ref}$	The d-axis and q-axis grid current references in the dq-frame.
I_{iS}, I_{iL}	Currents flowing into source and load parts at node $\#i$.
I_p, I_q, I_{p+q}	p, q , and $p + q$ -dimensional identity matrices.
K_{cp}	Capacitor-current-feedback coefficient.
K_{ppll}, K_{ipll}	Proportional and integral gains of the PLL regulator.
K_p, K_i	Proportional and integral gains of the current regulator.
L_{f1}, L_{f2}	Inverter-side and grid-side filter inductances.
s	Laplace operator.
V_{dc}	DC-link voltage.
V_g	Grid voltage (phase-to-phase RMS).
v_{inj}, i_{inj}	Small-signal voltage and current perturbations.
V_i	Voltage of node $\#i$.
X_{iS}, X_{iL}	State-variable vectors of source and load parts divided at node $\#i$.
Y_{iS}, Y_{iL}	Source and load admittances at node $\#i$.
$Z(\bullet), P(\bullet)$	Number of RHP zeros and RHP poles.
$Z_{iS}^{fit}, Z_{iL}^{fit}$	Fitted source and load impedances at

Z_A, Z_B, Z_C, Z_D	node $\#i$. Impedances of sub-modules A, B, C, and D.
Z_{iLIM}	Discrete frequency responses of the LIM derived at node i .
Z_{iLIM}^{fit}	Fitted frequency responses of the LIM derived at node i .
Z_{iS}, Z_{iL}	Source and load impedances at node $\#i$.
\mathbf{K}_{cpi}	i th collection of capacitor-current-feedback coefficients of the three GCIs.
$\lambda_{iSx}, \lambda_{iLy}$	x th eigenvalue of A_{iS} and y th eigenvalue of A_{iL} .
θ_g	Detected grid phase angle by PLL.
$A_{sys}^{11}, A_{sys}^{12}, A_{sys}^{21}, A_{sys}^{22}$	Four submatrices of A_{sys} .
$g_{1,2,\dots,6}$	Six switching signals.
$G_{del}, G_{del1}, G_{del2}$	Digital time delay $e^{-1.5T_s s}$.
G_i	Current controller.
$I_{g,dq}^{ref}$	Grid current reference in the dq-frame.
$I_{Cf,abc}, I_{Cf,dq}$	Capacitor currents in the abc-frame and dq-frame.
$I_{g,abc}, I_{g,dq}$	Grid currents in the abc-frame and dq-frame.
I_{iS_N}	Current source of the Norton equivalent circuit of source part at node $\#i$.
$N_{(-1,j0)}(\bullet)$	Counterclockwise encirclement number of the Nyquist plot around $-1+j0$ in complex plane.
$V_{c,abc}, V_{c,dq}$	Modulation voltages in the abc-frame and dq-frame.
V_{iL_T}	Voltage source of the Thevenin equivalent circuit of load part at node $\#i$.
$V_{PCC,abc}$	PCC voltages in the abc-frame.
Z_{GCI}, Z_g	Impedances of the GCI and the grid.

I. INTRODUCTION

Recently, the penetration level of renewable energies, such as wind power and photovoltaic power, in power systems has been continuously increasing [2], [3]. For example, the global cumulative installed renewable power capacity increased significantly from about 1050 GW in 2008 to about 2450 GW in 2018, accounting for more than 33% of the global total installed power generation capacity in 2018 [4], [5]. Specifically, 51% of the electric power generation in Denmark in 2018 was covered by wind power and solar power. Denmark aims to achieve 100% nonfossil-based power generation by 2050. Power electronic converters are widely adopted as an efficient interface between the dispersed generation units and the main grid, due to their superior efficiency, sustainability, and control flexibility [6]. However, impedance interactions between control loops of voltage source grid-connected inverters (GCIs) and weak grids may result in instability phenomena in wide frequency ranges [7], e.g., low-frequency instability phenomena related to outer power control loop [8]–[10], dc-link voltage control loop [11], and phase-locked loop (PLL) [12], high-frequency harmonic instability

phenomena related to inner current control loop [13], [14], and sideband oscillation of the switching frequency related to coupling dynamics of PWM and sampling process [15]. It is of importance to identify the instability phenomena and locate corresponding instability sources at the system design stage, which enables system stabilization by re-tuning the critical controller parameters [16].

Two main breeds of instability analysis approaches have been developed recently, i.e., state-space model (SSM)-based eigenvalues analysis [17]–[21] and impedance-based stability criterion (IBSC) [22]–[42]. In the SSM-based eigenvalues analysis method, eigenvalues of system state matrix are calculated, based on which system stability is assessed by checking whether real parts of any eigenvalues are positive [17]–[21]. Participation factors (PFs) of all state variables on unstable eigenvalues can further be computed, which enables the identification of critical controller parameters. However, the order of the system state matrix could be very high, if there exists a huge number of GCIs in the power systems, which will bring heavy computational burdens. Furthermore, internal structures and parameters of components are sometimes unknown for the system planner, due to industrial secrecy and intellectual property rights, which obstacles derivation of the system state matrix [16]. On the other hand, the whole power system is partitioned into load and source subsystems at a specific point by the IBSC, and the Nyquist criterion (NC) is applied on impedance ratio of the two subsystems to assess the stability at the selected point, where both encirclement number of Nyquist plot of the impedance ratio around $-1+j0$ in complex plane and number of right-half-plane (RHP) poles of the impedance ratio are calculated [22]. Since terminal impedance characteristics of GCIs can be obtained without knowing information about internal structure and parameters [34], the IBSC has widely been applied in inverter-fed power systems based on single GCI [8], [11], [12], [22], multi-paralleled GCIs [10], [13], [23]–[25], [29]–[31], and network-connected GCIs [27], [28], [32], [35]–[39]. The relation between the characteristics equation in the SSM-based eigenvalues analysis and poles and zeros of the impedance ratio in the IBSC is theoretically investigated in [43], which indicates that both methods can effectively assess the system stability. However, a two-terminal VSC-based HVdc system, as an example, is used to observe the differences between the two methods, which cannot reveal the generalized discrepancy in other power electronics-based power systems.

Avoidance of calculation of the number of RHP poles of impedance ratio and identification of instability sources are two main research interests of the IBSC. For single-GCI-based power systems, calculation of RHP poles is naturally avoided, since both the source and load subsystems are inherently stable, and no RHP poles exist [8], [11], [12], [22]. However, the number of RHP poles should be calculated for multi-paralleled and network-connected GCI systems, since RHP poles may emerge when component impedances are aggregated [25], [27], [28], [44]. In addition, instability sources cannot be identified if the IBSC is only performed one time at a specific point, e.g., point of common coupling (PCC), since components dynamics are missing in the aggregated

source and load impedance models [10], [23], [24]. In [27], [37]–[39], calculation of the number of RHP poles is avoided by calculating the encirclement numbers of Nyquist plots of impedance ratios at all nodes around $-1 + j0$ sequentially from the farthest node to PCC, and the nodes where the encirclement numbers are not zero are identified as instability sources. However, heavy computational burdens can be involved if a large number of nodes exist. In [28], [35], [36], components dq-frame impedance models are connected based on system topology, based on which the loop impedance model (LIM) is derived. Determinant of the LIM is then calculated to assess system stability. Calculation of the number of RHP poles is, thus, avoided. Instability sources, however, cannot be identified, since information of system structure is missing in the LIM [33]. In [29]–[32], information about system structure is maintained by the nodal admittance matrix (NAM). System stability can then be assessed by determinant of the NAM, and contributions of all components on modes of interest can be calculated by the PF analysis. However, when there exists a huge number of nodes, the order of the NAM is very high, and heavy computational burdens will be involved. In addition, instability sources can only be identified at component level instead of controller parameter level. Comparative analysis of the three stability criteria, e.g., the NC-based, the LIM-based, and the NAM-based methods, can be found in [33].

A set of discrete frequency responses are able to be fitted as either a continuous transfer function or an SSM by the vector fitting (VF) algorithm [45], [46]. Recently, the VF algorithm has initially been used to assess harmonic stability of inverter-fed power systems, where either calculation of RHP poles number is avoided or instability sources can be identified [44], [47], [48]. In [47], frequency scanning is performed at a specific node to obtain system apparent impedance which is actually the impedance frequency responses of the whole system at this node. System eigenvalues are then obtained by approximating the system apparent impedance into an SSM using the VF algorithm. However, problematic subsystems and components cannot further be identified, since the whole power system is regarded as a black box. In addition, the apparent impedance method is not applicable for an unstable system due to the prerequisite of frequency scanning. In [48], the SSMs of all components are first fitted from terminal impedance characteristics using the VF algorithm, based on which system SSM is obtained by combining these component SSMs according to their connection relationship [21]. Problematic components can be identified, and the method is applicable for an unstable system. However, the connection matrix of large-scale power systems is difficult to derive. In addition, the fitting errors of all components may be accumulated in the final system SSM, thus affecting stability analysis results [44]. In [47], [48], impedance frequency responses are actually translated into SSM for eigenvalues-based stability analysis. On the other hand, in [44], the number of RHP poles of impedance ratio is calculated by applying the VF algorithm directly on source and load impedance frequency responses, which actually facilitates the IBSC with the help of the VF algorithm. Problematic subsystems and components can be identified in [44] and [48], respectively. However,

problematic controller parameters cannot be further located, since the components are treated as black boxes. Recently, internal circuit and controller parameters of the GCI are identified from terminal impedance frequency responses using system identification technology with internal structure known, which enables further instability source location at controller parameter level [1], [16].

To further explore the capability of the VF algorithm in stability analysis and corresponding instability sources identification, which has initially been investigated in [44], [47], [48]. This paper presents a gray-box hierarchical instability source identification method of the multiple-inverter-fed power systems, which enables stability analysis at system, component, and parameter levels sequentially. At system level, terminal impedance frequency responses of all components, e.g., GCIs, transmission lines, and transformers, are first measured using frequency scanning method. The impedance network model (INM) is then established by connecting these individual components based on system topology, which is further lumped into the LIM. System SSM is then generated from impedance frequency responses of the LIM using the VF algorithm for eigenvalues analysis. At component level, if the system is assessed to be unstable, problematic components are further identified by performing the NC at terminals of all components, where the numbers of RHP poles are obtained by the VF algorithm. Finally, at parameter level, circuit and controller parameters of the identified problematic components are further identified using the VF algorithm, so that critical controller parameters can be re-tuned to improve system stability. It can be seen that the VF algorithm is applied in all three steps. Compared with the aforementioned existing works, the contributions of this paper are fourfold. 1) Referring to [43], the commonalities and discrepancies between the SSM-based eigenvalues analysis and the IBSC are theoretically derived, based on which feasibility and limitation of the LIM for system stability analysis are analyzed. 2) Referring to [28], [33], [35], [36], a non-parametric LIM-based eigenvalues identification method using the VF algorithm is proposed, which enables global stability analysis with only components impedance frequency responses known. 3) Referring to [44], [47], [48], a problematic components identification method by using the NC at terminals of all components is shown, where calculation of the number of RHP poles is facilitated by the VF algorithm. 4) Referring to [16], a VF algorithm-based parameters identification method of GCI based on terminal impedance characteristics is presented, where only information about internal structure is necessary.

The rest of this paper is organized as follows. In Section II, theoretical basis of the proposed method is explained. The principle of the proposed gray-box hierarchical instability source identification method is explained in Section III. In Section IV, the proposed stability analysis method is implemented in a multiple-paralleled GCI system. Simulation results obtained in Matlab/Simulink platform and real-time verification results obtained in OPAL-RT platform are provided in Section V to validate the effectiveness of the proposed stability analysis method. Finally, conclusions are drawn in Section VI.

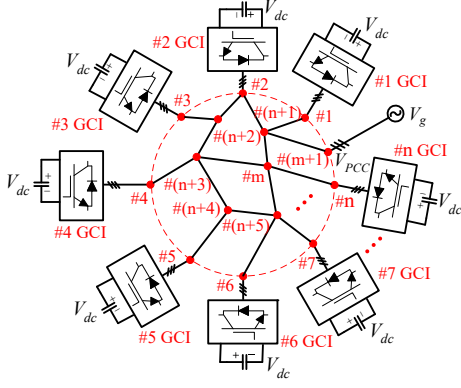


Fig. 1. Conceptual diagram of a power plant which consists of multiple GCIs coupled via a complicated transmission network [49].

II. THEORETICAL BASIS

In this section, the NC-based, the eigenvalues-based, and the LIM-based stability analysis methods are first introduced, where the commonalities and discrepancies among them are also discussed. In addition, the principle of the VF algorithm is explained. Next, the pole-zero cancellation issue during the impedance aggregation procedure is shown, where the method to identify the pole-zero cancellation phenomena and corresponding countermeasure to avoid this issue are also discussed.

A. Relation of Three Stability Analysis Methods

Fig. 1 shows the conceptual diagram of a multiple-inverterfed power system, where the inverters are coupled via a complicated transmission network [49]. n GCIs exist in the power system, and their terminal nodes are labeled as #1, #2, ..., #n, respectively. Other $m - n$ nodes located inside the red dashed circle are labeled as # $(n + 1)$, # $(n + 2)$, ..., # m , respectively. In addition, PCC is labeled as node # $(m + 1)$.

1) *NC-Based Stability Analysis Method:* The whole power system in Fig. 1 is partitioned into two subsystems, i.e., source part and load part, at a specific node # i ($i \in [1, m + 1]$), as shown in Fig. 2(a). The SSMs of source and load parts can be represented as

$$\begin{aligned} \frac{d\Delta X_{iS}}{dt} &= A_{iS}\Delta X_{iS} + B_{iS}\Delta V_i \\ \Delta I_{iS} &= C_{iS}\Delta X_{iS} + D_{iS}\Delta V_i \end{aligned} \quad (1)$$

$$\begin{aligned} \frac{d\Delta X_{iL}}{dt} &= A_{iL}\Delta X_{iL} + B_{iL}\Delta I_{iL} \\ \Delta V_i &= C_{iL}\Delta X_{iL} + D_{iL}\Delta I_{iL} \end{aligned} \quad (2)$$

where X_{iS} and X_{iL} are $(p \times 1)$ -dimensional and $(q \times 1)$ -dimensional state-variable vectors of source and load parts, respectively. A_{iS} , B_{iS} , C_{iS} , and D_{iS} are $p \times p$, $p \times 1$, $1 \times p$, and 1×1 matrices, respectively. In addition, A_{iL} , B_{iL} , C_{iL} , and D_{iL} are $q \times q$, $q \times 1$, $1 \times q$, and 1×1 matrices, respectively. Y_{iS} and Z_{iL} can be derived from (1) and (2), shown as

$$Y_{iS} = \frac{\Delta I_{iS}}{\Delta V_i} = C_{iS}(sI_p - A_{iS})^{-1}B_{iS} + D_{iS} \quad (3)$$

$$Z_{iL} = \frac{\Delta V_i}{\Delta I_{iL}} = C_{iL}(sI_q - A_{iL})^{-1}B_{iL} + D_{iL} \quad (4)$$

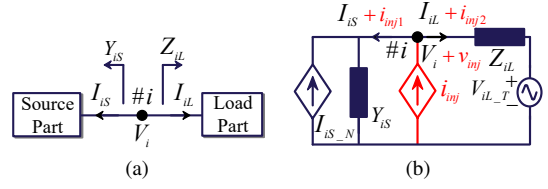


Fig. 2. Derivation of the NC-based and the LIM-based stability analysis methods from the SSM-based eigenvalues analysis method. (a) Partition of Fig. 1 into source part and load part at node # i . (b) Equivalent circuit representation of source part and load part.

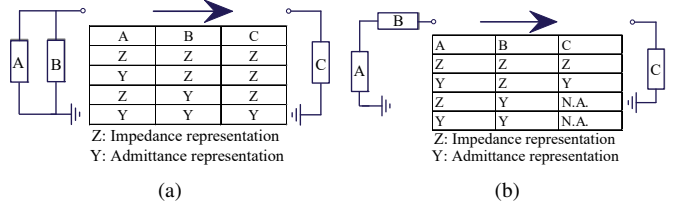


Fig. 3. Aggregation rules of two sub-modules. (a) Parallel connection. (b) Series connection.

where I_p and I_q are the p -dimensional and q -dimensional identity matrices, respectively. The source and load parts can then be modeled as the Norton and the Thevenin equivalent circuits, respectively, shown as Fig. 2(b).

In detail, the principle of physical separation of the whole power plant in Fig. 1 into two parts in Fig. 2 is explained here. The aggregation rules of two sub-modules are defined as

- 1) The GCIs are regarded as Y-type sub-modules. In addition, the grid is regarded as a Z-type sub-module [22].
- 2) The transmission lines can be regarded as either Y-type or Z-type sub-modules. In detail, the transmission line is regarded as a Y-type sub-module in parallel connection case and a Z-type sub-module in series connection case, respectively.
- 3) The type of the aggregated sub-module C can be identified based on the types of sub-modules A and B, shown as [27], [50]

$$\begin{aligned} A_Z \Theta B_Z &= A_Z \oplus B_Z = C_Z \\ A_Y \Theta B_Y &= A_Y \oplus B_Z = C_Y \\ A_Z \Theta B_Y &= A_Y \Theta B_Z = C_Z \end{aligned} \quad (5)$$

where Θ and \oplus are parallel and series connection operators, respectively. The subscripts Z and Y indicate that the sub-module is Z-type and Y-type, respectively. The aggregation rules in (5) are summarized in Fig. 3.

- 4) Y-type and Z-type sub-modules should be modeled as the Norton and Thevenin equivalent circuits, respectively.

It can be concluded from 1)- 4) that by dividing the whole power plant in Fig. 1 into two parts at an arbitrary node, e.g., the n terminal nodes of the n GCIs, the $m - n$ nodes located inside the red dashed circle, or the PCC node, the part which consists of the grid is physically identified as the load part, and modeled as the Thevenin equivalent circuit. In addition, the other part is physically identified as the source part, and modeled as the Norton equivalent circuit.

According to the basic circuit principle, current flowing through the checking node $\#i$ in Fig. 2(b) can be calculated as [22]

$$I_{iL} = \frac{I_{iS_N} - V_{iL_T} Y_{iS}}{1 + Z_{iL} Y_{iS}} \quad (6)$$

Since both the source and load parts cannot be guaranteed to be inherently stable, the RHP poles of I_{iL} should be assessed by checking whether $1 + Z_{iL} Y_{iS}$ has any RHP zeros and $I_{iS_N} - V_{iL_T} Y_{iS}$ has any RHP poles, i.e., [50]

$$\begin{aligned} P(I_{iL}) &= Z(1 + Z_{iL} Y_{iS}) + P(I_{iS_N} - V_{iL_T} Y_{iS}) \\ &= P(Z_{iL} Y_{iS}) - N_{(-1, j0)}(Z_{iL} Y_{iS}) \dots \\ &\quad + P(I_{iS_N} - V_{iL_T} Y_{iS}) \end{aligned} \quad (7)$$

where $Z(\bullet)$ and $P(\bullet)$ indicate the numbers of RHP zeros and RHP poles, respectively. $N_{(-1, j0)}(\bullet)$ indicates the counterclockwise encirclement number of the Nyquist plot around $-1 + j0$ in complex plane.

Since Y_{iS} and I_{iS_N} share the same poles, and Z_{iL} and V_{iL_T} share the same poles [14], (7) can be reformulated as

$$P(I_{iL}) = \underbrace{P(Z_{iL})}_{\text{Internal stability}} + \underbrace{P(Y_{iS})}_{\text{stability}} - \underbrace{N_{(-1, j0)}(Z_{iL} Y_{iS})}_{\text{Interactive stability}} \quad (8)$$

It can be seen from (8) that the stability of I_{iL} is dependent on two parts, i.e., the internal stability which is determined by the aggregated models of source and load parts, and the interactive stability which is determined by the impedance interactions between the source and load parts.

2) *Eigenvalues-Based Stability Analysis Method*: The power system in Fig. 1, as a whole, can be represented as a linearized SSM, shown as

$$\frac{d\Delta X_{sys}}{dt} = A_{sys} \Delta X_{sys} \quad (9)$$

where $X_{sys} = [X_{iS}, X_{iL}]^T$. X_{sys} and A_{sys} are $(p+q) \times 1$ -dimensional state-variables vector and $(p+q) \times (p+q)$ -dimensional system state matrix, respectively. System stability can be checked based on the eigenvalues of A_{sys} which can be obtained by combing the two small SSMs in (1) and (2), show as [21]

$$\begin{aligned} \frac{d\Delta X_{sys}}{dt} &= \left[\begin{array}{c} \frac{d\Delta X_{iS}}{dt} \\ \frac{d\Delta X_{iL}}{dt} \end{array} \right] = A_{sys} \Delta X_{sys} \\ &= \left[\begin{array}{cc} A_{sys}^{11} & A_{sys}^{12} \\ A_{sys}^{21} & A_{sys}^{22} \end{array} \right] \left[\begin{array}{c} \Delta x_{iS} \\ \Delta x_{iL} \end{array} \right] \end{aligned} \quad (10)$$

where A_{sys}^{11} , A_{sys}^{12} , A_{sys}^{21} , and A_{sys}^{22} are

$$\begin{aligned} A_{sys}^{11} &= A_{iS} - B_{iS}(1 + D_{iL} D_{iS})^{-1} D_{iL} C_{iS} \\ A_{sys}^{12} &= B_{iS}(1 + D_{iL} D_{iS})^{-1} C_{iL} \\ A_{sys}^{21} &= -B_{iL}(1 + D_{iL} D_{iS})^{-1} C_{iS} \\ A_{sys}^{22} &= A_{iL} - B_{iL}(1 + D_{iL} D_{iS})^{-1} D_{iS} C_{iL} \end{aligned} \quad (11)$$

The characteristics equation can then be calculated as

$$\left| sI_{p+q} - \left[\begin{array}{cc} A_{sys}^{11} & A_{sys}^{12} \\ A_{sys}^{21} & A_{sys}^{22} \end{array} \right] \right| = 0 \quad (12)$$

where I_{p+q} is the $(p+q)$ -dimensional identity matrix. According to the detailed derivation process in Appendix A, (12) can be reformulated as

$$\underbrace{\prod_{x=1}^p (s - \lambda_{iSx})}_{\text{Internal stability}} \underbrace{\prod_{y=1}^q (s - \lambda_{iLy})}_{\text{stability}} \underbrace{\frac{(1 + D_{iL} Y_{iS})^{p-q}}{(1 + D_{iL} D_{iS})^p} (1 + Z_{iL} Y_{iS})^q}_{\text{Interactive stability}} = 0 \quad (13)$$

where λ_{iSx} ($x \in [1, p]$) and λ_{iLy} ($y \in [1, q]$) are the p and q eigenvalues of A_{iS} and A_{iL} , respectively.

It can be intuitively seen from (8) and (13) that the identified RHP solutions of the NC-based and eigenvalues-based stability analysis methods are the same, which indicates that the two methods can achieve the same global stability analysis conclusions. However, the discrepancy of the RHP solutions of (8) and (13) will exist if at least one subsystem of source and load parts has RHP poles, i.e., $\exists x \in [1, p], \text{real}(\lambda_{iSx}) > 0$ or $\exists y \in [1, q], \text{real}(\lambda_{iLy}) > 0$, and the RHP poles are canceled out in the formulation of Z_{iL} and Y_{iS} . In this case, only local stability analysis results can be obtained by the NC-based analysis method. To obtain the global stability analysis result, the NC should be performed at another node, or another impedance aggregation path should be selected, as explained in Section II-C. Therefore, only one node needs to be considered for stability study using the NC, if there is no pole-zero cancellation happens. Otherwise, additional nodes should further be considered. As for the eigenvalues-based stability study, all nodes should be considered to structurally build the SSM of the whole system [48].

3) *LIM-Based Stability Analysis Method*: LIM can be obtained by injecting a small current disturbance i_{inj} into a specific node and observing voltage response v_{inj} at this node (The LIM is also called as the apparent impedance in [47]). The schematic diagram is shown as Fig. 2(b). The LIM of the whole system can be calculated as

$$Z_{iLIM} = \frac{v_{inj}}{i_{inj}} = \frac{v_{inj}}{i_{inj1} + i_{inj2}} = \frac{Z_{iL}}{1 + Z_{iL} Y_{iS}} \quad (14)$$

Similar with (7), the number of the RHP poles of Z_{iLIM} can be calculated as

$$\begin{aligned} P(Z_{iLIM}) &= Z(1 + Z_{iL} Y_{iS}) + P(Z_{iL}) \\ &= \underbrace{P(Z_{iL})}_{\text{Internal stability}} + \underbrace{P(Y_{iS})}_{\text{stability}} - \underbrace{N_{(-1, j0)}(Z_{iL} Y_{iS})}_{\text{Interactive stability}} \end{aligned} \quad (15)$$

Similar with the NC-based stability analysis method, if no pole-zero cancellation happens, the poles of Z_{iLIM} are equal to the eigenvalues of A_{sys} , which indicates the feasibility of the LIM for stability analysis.

B. VF Algorithm

A set of discrete impedance frequency responses can be fitted as a continuous transfer function in form of partial

fraction expansion representation or polynomial representation using the VF algorithm, shown as [45], [46]

$$f(s) = \sum_{i=0}^M \frac{R_i}{s - \lambda_i} + D + Es \quad (16)$$

$$f(s) = \left(\sum_{i=0}^M B_i s^i \right) / \left(\sum_{i=0}^M A_i s^i \right) + Es \quad (17)$$

where λ_i and R_i are the i th pole and residue, respectively. M is the order of the fitted transfer function, which can be determined in a trial-and-error way. The fitted transfer function in form of (16) will be used to identify RHP poles for system-level and component-level stability analysis. In addition, the fitted transfer function in form of (17) will be used to identify the circuit and controller parameters of the GCI for parameter-level stability analysis.

C. Pole-Zero Cancellation Phenomena During Impedance Aggregation Procedure

Controllability and observability are two major features of a linear control system [51]. Controllability is the ability to manipulate the vector of state variables from an initial state to any arbitrary value in finite time by setting a suitable input variable. In addition, observability defines the ability to determine the initial state of a system from finite observation of the output. The following theorems are satisfied for a linear system [52].

Theorem 1: A linear system is controllable and observable if and only if there is no pole-zero cancellation in the transfer function representation.

Theorem 2: The series and parallel connections of two linear systems are controllable and observable if and only if transfer function representations of the two systems have no pole-zero cancellation.

The individual component, e.g., GCI, transmission line, and transformer, is controllable and observable. According to theorem 1, there is, therefore, no pole-zero cancellation in terminal impedance transfer function. In addition, the actual power system is almost always controllable and observable [36]. According to theorem 2, there is, therefore, no pole-zero cancellation of aggregated terminal impedance transfer functions. Therefore, system modes can be preserved in the established LIM. For the rarely-existed uncontrollable or unobservable power systems, if pole-zero cancellation phenomena are identified when component impedances are aggregated, another aggregation path should be selected [33]. In detail, the method to identify the pole-zero cancellation phenomena and corresponding countermeasure to avoid this issue are discussed as follows.

1) *Identification of the Pole-Zero Cancellation Phenomena:* As shown in Fig. 3, there are two basic connection relations between two sub-modules, i.e., parallel connection and series

connection. The impedance representations of sub-modules A and B can be generally formulated as

$$Z_A = \frac{N_A}{D_A} = \frac{\prod_{i=1}^{m_1} (s - \gamma_{1i})(s - \gamma_{1i}^*) \prod_{j=1}^{n_1} (s - \gamma_{1j})}{s^{k_1} \prod_{r=1}^{p_1} (s - \lambda_{1r})(s - \lambda_{1r}^*) \prod_{t=1}^{q_1} (s - \lambda_{1t})}$$

$$Z_B = \frac{N_B}{D_B} = \frac{\prod_{i=1}^{m_2} (s - \gamma_{2i})(s - \gamma_{2i}^*) \prod_{j=1}^{n_2} (s - \gamma_{2j})}{s^{k_2} \prod_{r=1}^{p_2} (s - \lambda_{2r})(s - \lambda_{2r}^*) \prod_{t=1}^{q_2} (s - \lambda_{2t})} \quad (18)$$

where γ_{1i} and γ_{1i}^* , γ_{2i} and γ_{2i}^* are conjugate zeros of Z_A and Z_B , respectively. γ_{1j} and γ_{2j} are real zeros of Z_A and Z_B , respectively. In addition, λ_{1r} and λ_{1r}^* , λ_{2r} and λ_{2r}^* are conjugate poles of Z_A and Z_B , respectively. λ_{1t} and λ_{2t} are real poles of Z_A and Z_B , respectively.

Assume that A and B are connected in parallel. The impedance of the aggregated sub-module C can be derived as

$$Z_C = \frac{N_C}{D_C} = \frac{Z_A Z_B}{Z_A + Z_B} = \frac{N_A N_B}{N_A D_B + N_B D_A} \quad (19)$$

If Z_A and Z_B have the same RHP zero, e.g., $\exists j \in \min(n_1, n_2)$, $\gamma_{1j} = \gamma_{2j} = \gamma_0$, and $real(\gamma_0) > 0$, Z_C can be reformulated as

$$Z_C = \frac{N_C}{D_C} = \frac{(s - \gamma_0)^2 N'_A N'_B}{(s - \gamma_0) N'_A D_B + (s - \gamma_0) N'_B D_A} \quad (20)$$

Where $N'_A = N_A / (s - \gamma_0)$ and $N'_B = N_B / (s - \gamma_0)$. The pole-zero cancellation happens in (20). Therefore, Z_C can further be simplified as

$$Z_C = \frac{N'_C}{D'_C} = \frac{(s - \gamma_0) N'_A N'_B}{N'_A D_B + N'_B D_A} \quad (21)$$

It can be seen from (20) and (21) that $D_C = (s - \gamma_0) D'_C$, i.e., the RHP pole γ_0 of Z_C is lost due to the pole-zero cancellation.

On the other hand, assume that A and B are connected in series. The impedance of the aggregated sub-module D can be derived as

$$Z_D = \frac{N_D}{D_D} = Z_A + Z_B = \frac{N_A D_B + N_B D_A}{D_A D_B} \quad (22)$$

If Z_A and Z_B have the same RHP pole, e.g., $\exists t \in \min(q_1, q_2)$, $\lambda_{1t} = \lambda_{2t} = \lambda_0$, and $real(\lambda_0) > 0$, Z_C can be reformulated as

$$Z_D = \frac{N_D}{D_D} = \frac{N_A (s - \lambda_0) D'_B + N_B (s - \lambda_0) D'_A}{(s - \lambda_0)^2 D'_A D'_B} \quad (23)$$

where $D'_A = D_A / (s - \lambda_0)$ and $D'_B = D_B / (s - \lambda_0)$. Similar with (20), the pole-zero cancellation happens in (23). Therefore, Z_D can further be simplified as

$$Z_D = \frac{N'_D}{D'_D} = \frac{N_A D'_B + N_B D'_A}{(s - \lambda_0) D'_A D'_B} \quad (24)$$

Slightly different from (21), the RHP pole λ_0 is preserved in D'_D . However, compared with D_D , the order of D'_D is reduced due to the pole-zero cancellation.

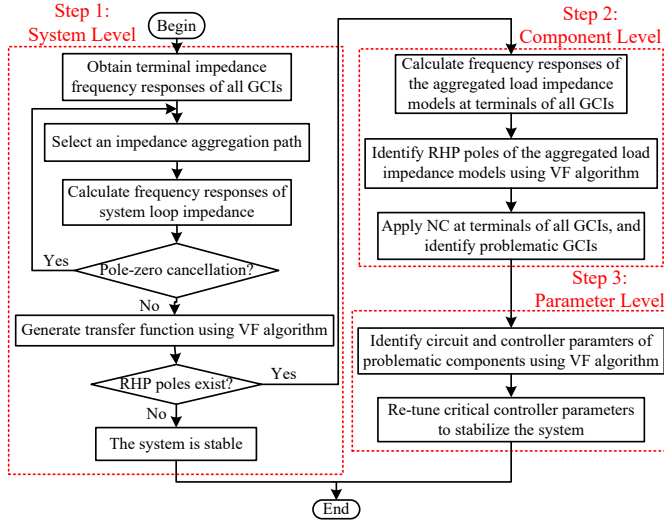


Fig. 4. Flowchart of the proposed gray-box hierarchical instability source identification method.

Since each pair of conjugate complex poles of Z_A and Z_B in (18) corresponds to a peak in the magnitude-frequency response curve, and each pair of conjugate complex zeros corresponds to a valley [53], the practical method to identify the pole-zero cancellation phenomena can be explained as follows. For the parallel connection, if the magnitude-frequency response curves of Z_A and Z_B have the valleys at the same frequency, and the aggregated magnitude-frequency response curve does not have the peak at the frequency, the pole-zero cancellation happens. For the series connection, if the magnitude-frequency response curves of Z_A and Z_B have the peaks at the same frequency, and the aggregated magnitude-frequency response curve does not have the valley at the frequency, the pole-zero cancellation happens.

2) Avoidance of the Pole-Zero Cancellation Phenomena:

According to the aforementioned analysis of the pole-zero cancellation, corresponding countermeasure to avoid these phenomena during the impedance aggregation can be presented, i.e., avoid aggregating two parallel-connected subsystems which have the same valleys of magnitude-frequency response curves, and avoid aggregating two series-connected subsystems which have the same peaks of magnitude-frequency response curves. Specifically, they can be achieved by selecting another impedance aggregation path and another checking node, respectively.

III. PROPOSED HIERARCHICAL INSTABILITY SOURCE IDENTIFICATION METHOD

In this section, flowchart of the proposed gray-box hierarchical instability source identification method is first given, followed by explanation of each step in detail.

Fig. 4 shows the flowchart of the proposed instability source identification method which consists of three main steps, i.e., stability analysis at system level (Step 1), component level (Step 2), and parameter level (Step 3).

A. Step 1: System-Level Stability Analysis

Terminal impedance frequency responses of all GCIs are first measured using the frequency scanning method or obtained from manufacturers. Frequency responses of system LIM at a specific node are then calculated based on a selected impedance aggregation path. If pole-zero cancellation happens during the impedance aggregation process, another impedance aggregation path is selected, and frequency responses of the system LIM are re-calculated. System transfer function in form of (17) is then generated from the frequency responses of the system LIM using the VF algorithm. If the fitted transfer function does not have any RHP poles, the system is assessed as stable, and no further steps will be performed. Otherwise, the system is assessed as unstable, and steps 2 and 3 will be performed.

B. Step 2: Component-Level Stability Analysis

The NC is performed at all nodes to identify the problematic components. For example, frequency responses of the aggregated load impedance models at terminals of all GCIs are calculated based on the terminal impedance frequency responses measured in step 1. Transfer function in form of (16) is then fitted using the VF algorithm, and the RHP poles of the fitted transfer function are then identified. Finally, NC is applied at terminals of all GCIs, where the number of unstable modes is calculated based on NC in (7). The GCIs where NC is not satisfied are identified as problematic components.

C. Step 3: Parameter-Level Stability Analysis

Terminal impedance frequency responses of the identified problematic GCIs are fitted as transfer functions in form of (17) using the VF algorithm. Then, circuit and controller parameters of the problematic GCIs are identified by comparing the fitted and theoretical impedance transfer functions. On the basis of it, the identified critical controller parameters are re-tuned to improve system stability.

A GCI with capacitor-current-feedback active damping is taken as an example to illustrate the principle of the proposed gray-box circuit and controller parameters identification method. The control diagram is shown in Fig. 5(a), where LCL filter is used to attenuate the high-frequency switching harmonics. PLL is used to synchronize the phase angle of injected current with PCC voltage. The capacitor-current proportional feedback active damping K_{cp} is used to suppress the LCL filter resonance peak [54]. $G_i = K_p + \frac{K_i}{s}$ is the PI controller of current control loop in dq reference frame. $G_{del} = e^{-1.5T_s s}$ represents time delay including 1.0 T_s digital computation delay and 0.5 T_s PWM delay (T_s is the sampling period). When PLL bandwidth is low enough, influence of PLL dynamics on output impedance can be ignored [8]. The d-axis control and q-axis control are decoupled and identical. Fig. 5(b) shows the d-axis control block diagram, based on which output impedance can be derived as [1], [54]

$$Z_{GCI}(s) = \frac{L_{f1}s + G_i G_{del1}}{L_{f1}C_f s^2 + K_{cp}C_f G_{del2}s + 1} + L_{f2}s \quad (25)$$

where $G_{del1} = G_{del2} = e^{-1.5T_s s}$.

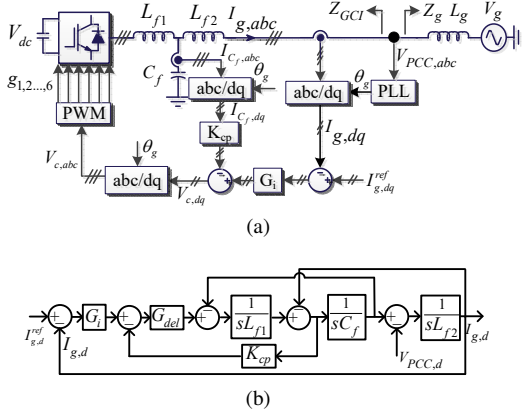


Fig. 5. Topology and control block diagram of the LCL-filtered GCI with capacitor-current-feedback active damping. (a) System topology. (b) The d-axis control block diagram [54].

To identify the circuit and controller parameters of the GCI from its terminal impedance formula, $e^{-1.5T_s s}$ in (25) should be represented by Pade approximation with appropriate order, so that (25) can be in the same form of (17), and the parameters can be identified by equalizing their coefficients. For example, G_{del1} can be approximated as [20]

$$G_{del1} \approx \frac{b_0 + \dots + b_i s^i + \dots + b_{v_1} s^{v_1}}{a_0 + \dots + a_j s^j + \dots + a_{u_1} s^{u_1}} \quad (26)$$

where $a_j = \frac{(v_1+u_1-j)!u_1!}{j!(u_1-j)!}(1.5T_s)^j$ ($j \in [0, u_1]$) and $b_i = (-1)^i \frac{(v_1+u_1-i)!v_1!}{i!(v_1-i)!}(1.5T_s)^i$ ($i \in [0, v_1]$).

Similarly, G_{del2} can be approximated as

$$G_{del2} \approx \frac{d_0 + \dots + d_i s^i + \dots + d_{v_2} s^{v_2}}{c_0 + \dots + c_j s^j + \dots + c_{u_2} s^{u_2}} \quad (27)$$

where $c_j = \frac{(v_2+u_2-j)!u_2!}{j!(u_2-j)!}(1.5T_s)^j$ ($j \in [0, u_2]$) and $d_i = (-1)^i \frac{(v_2+u_2-i)!v_2!}{i!(v_2-i)!}(1.5T_s)^i$ ($i \in [0, v_2]$).

(25) can be reformulated in form of (17) by substituting (26) and (27), shown as

$$Z_{GCI}(s) \approx \frac{\dots + F_1 s + F_0}{\dots + E_1 s + E_0} + L_{f2} s \quad (28)$$

where only several low-order components are shown for simplification. The detailed formulas are shown as

$$\begin{aligned} F_1 &= \frac{L_{f1}^2}{K_{cp} C_f} a_0 c_0 + \frac{K_p L_{f1}}{K_{cp} C_f} b_0 c_1 + \frac{K_p L_{f1}}{K_{cp} C_f} b_1 c_0 \\ E_1 &= L_{f1} a_0 d_0 + \frac{L_{f1}}{K_{cp} C_f} a_0 c_1 + \frac{L_{f1}}{K_{cp} C_f} a_1 c_0 \\ F_0 &= \frac{K_p L_{f1}}{K_{cp} C_f} b_0 c_0 \quad E_0 = \frac{L_{f1}}{K_{cp} C_f} a_0 c_0 \end{aligned} \quad (29)$$

It can be calculated from (17), (25), and (29) that,

$$L_{f2} = E \quad K_p = \frac{F_0}{E_0} = \frac{B_0}{A_0} \quad (30)$$

$$\begin{aligned} \frac{F_1}{E_0} &= \frac{B_1}{A_0} = L_{f1} + K_p \left(\frac{c_1}{c_0} + \frac{b_1}{a_0} \right) \\ \frac{E_1}{E_0} &= \frac{A_1}{A_0} = K_{cp} C_f + \frac{c_1}{c_0} + \frac{a_1}{a_0} \end{aligned} \quad (31)$$

On the other hand, it can be seen from (26) that,

$$\frac{a_1}{a_0} = \frac{1.5u_1}{u_1 + v_1} T_s \quad \frac{b_1}{a_0} = -\frac{1.5v_1}{u_1 + v_1} T_s \quad (32)$$

By substituting $b_1/a_0 = -v_1 a_1/u_1 a_0$ into (31), a_1/a_0 can also be expressed as

$$\frac{a_1}{a_0} = \frac{u_1}{u_1 + v_1} \left(\frac{A_1}{A_0} + \frac{L_{f1}}{K_p} - \frac{B_1}{A_0 K_p} - K_{cp} C_f \right) \quad (33)$$

By combining (32) and (33), we have

$$\frac{L_{f1}}{K_p} - K_{cp} C_f - 1.5T_s = \frac{B_1}{K_p A_0} - \frac{A_1}{A_0} \quad (34)$$

It can be seen from (34) that the identified circuit and controller parameters are independent on the selected orders of the Pade approximations, i.e., u_1 and v_1 in (26), u_2 and v_2 in (27).

In addition, the output impedance formula can be expressed in frequency-domain by substituting $s = j\omega$ into (25), shown as (59) in Appendix B. (59) can be reformulated as

$$Z_{GCI}(\omega) = \frac{B(\omega) + jC(\omega)}{A(\omega)} \quad (35)$$

where

$$\begin{aligned} A(\omega) &= (1 - L_{f1} C_f \omega^2 + K_{cp} C_f \omega \sin(1.5\omega T_s))^2 \dots \\ &\quad + (K_{cp} C_f \omega \cos(1.5\omega T_s))^2 \\ B(\omega) &= ((K_{cp} - K_p) C_f L_{f1} \omega^2 + K_p) \cos(1.5\omega T_s) \\ C(\omega) &= L_{f1}^2 L_{f2} C_f^2 \omega^5 + ((K_{cp} C_f)^2 L_{f2} - 2L_{f1} L_{f2} C_f \dots \\ &\quad - L_{f1}^2 C_f) \omega^3 + (L_{f1} + L_{f2} - K_{cp} K_p C_f) \omega + \dots \\ &\quad (-2K_{cp} L_{f1} L_{f2} C_f^2 \omega^4 + ((K_{cp} + K_p) C_f L_{f1} + \dots \\ &\quad 2K_{cp} C_f L_{f2}) \omega^2 - K_p) \sin(1.5\omega T_s) \end{aligned} \quad (36)$$

Since $A(\omega) > 0$, the derivative of $\angle Z_{GCI}(\omega)$ is calculated as

$$\frac{d\angle Z_{GCI}(\omega)}{d\omega} = \left(\arctan\left(\frac{C(\omega)}{B(\omega)}\right) \right)' = \frac{\left(\frac{C(\omega)}{B(\omega)}\right)'}{1 + \left(\frac{C(\omega)}{B(\omega)}\right)^2} \quad (37)$$

If the derivative of $\angle Z_{GCI}(\omega)$ is zero at ω_c , which can be observed from the phase diagram of the fitted transfer function $f(s)$ in (17), another constraint can be obtained with K_p and L_{f2} identified by (30), shown as

$$\left. \left(\frac{C(\omega)}{B(\omega)} \right)' \right|_{\omega=\omega_c} = 0 \quad (38)$$

By combining (34) and (38), the three unknown parameters (L_{f1} , C_f , and K_{cp}) can be identified using a trial-and-error method. Based on the identified circuit and controller parameters, system stability can be improved by re-tuning critical controller parameters.

D. Practical Implementation of the Proposed Gray-Box Hierarchical Instability Source Identification Method in Real-World Scenarios

In practice, the system planner such as the power grid company commonly installs an interconnected system which consists of various components provided by different vendors or manufacturers, e.g., GCIs, transmission lines/cables, and transformers. Although individual component is inherently stable, the interconnected system may become unstable due to undesired impedance interactions among these components. Therefore, the system planner hopes to identify the potential instability phenomena at the initial system design stage, and locate corresponding instability sources. However, detailed circuit and controller parameters of these components cannot normally be accessed by the system designer in the real world, due to the intellectual property right and industrial competence. Instead, these vendors and manufacturers probably only provide terminal impedance frequency responses or gray-box models of these components. In this case, theoretical derivation of the system SSM cannot be performed, so that the eigenvalues-based stability analysis method is not possible. For the stability analysis of single-GCI-based power systems, the provided discrete terminal impedance frequency responses are enough for the NC, since both source and load parts are inherently stable, i.e., $P(Z_{iL}) = P(Y_{iS}) = 0$ in (8) [22]. However, for the stability analysis of multi-GCI-based power systems in Fig. 1, the continuous transfer function representations of the terminal impedance characteristics are needed to calculate the RHP poles of both source and load parts, since RHP poles may emerge when component impedances are aggregated [33]. Therefore, a practical issue arises in real-world scenarios, i.e., how to perform stability analysis and locate corresponding instability sources in multi-GCI-based power systems based on only the discrete impedance frequency responses of various components provided by different vendors and manufacturers?

To better share the gray-box models among the system planner and vendors, and extract the stability characteristics of the interconnected power system from these gray-box models, this paper presents a gray-box hierarchical instability source identification method of multi-GCI-based power systems, as shown in Sections III-A, III-B, and III-C. In detail, the VF algorithm, as a powerful curve fitting tool, is used to fit the discrete impedance frequency responses into continuous transfer functions in all of the three steps, i.e., system-level, component-level, and parameter-level stability analysis. One real-world scenario where the gray-box method proposed in this paper can be applied is replicated here. Multiple vendors or manufacturers deliver the gray-box models to the power grid company at the initial design stage. Based on the terminal impedance frequency responses of all components, the power grid company can perform stability analysis at system and component levels with the help of the VF algorithm. Therefore, the problematic components which result in the instability phenomena can be located. In addition, the power grid company can further identify the circuit and controller parameters of the problematic components by equaling the fitted impedance transfer function using the VF algorithm

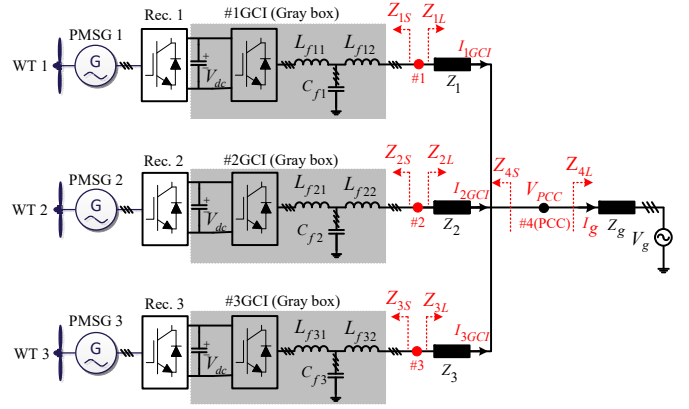


Fig. 6. Circuit configuration of the studied multi-paralleled GCI system.

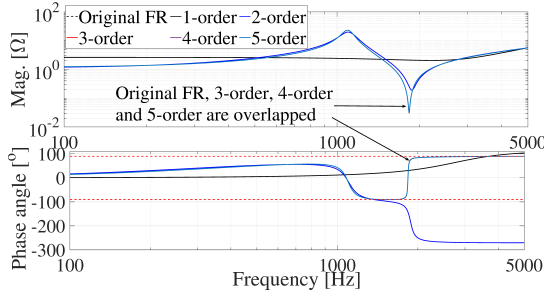
with the analytical terminal impedance formulas. In Section III-C, the circuit and controller parameters of the GCI with capacitor-current-feedback active damping are identified using the proposed method. Similar parameters extraction procedure can be performed for the GCIs under other control strategies, except that the analytical impedance model in (25) should be updated [16], [55]. With the instability source identification results, the power grid company can provide detailed feedback to the vendors or manufacturers, so that the problematic controller parameters can be re-tuned to improve stability of the interconnected power system. In fact, the presented method in this paper facilitates the cooperation between the power grid company as the system integrator and the vendors as the equipment suppliers to avoid potential instability phenomena by only sharing the gray-box models.

IV. IMPLEMENTATION OF THE PROPOSED INSTABILITY SOURCE IDENTIFICATION METHOD

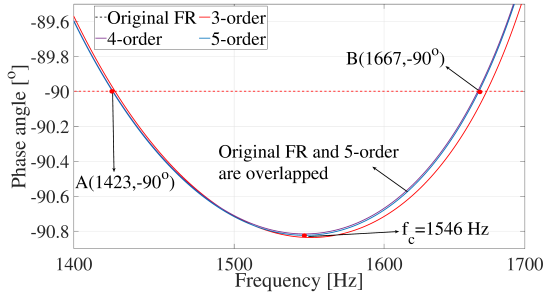
In this section, the proposed hierarchical instability source identification method is implemented in a simplified but representative multi-paralleled GCI system shown in Fig. 6, where the three GCIs are regarded as gray boxes. The inner current control loop-induced high-frequency harmonic instability phenomena are investigated first. Then, the further application of the proposed method for low-frequency instability source identification is discussed.

The per-unit-length (p.u.l.) resistance and inductance of the transmission lines in Fig. 6 are $10 \mu\Omega/\text{km}$ and $10 \mu\text{H}/\text{km}$, respectively. In addition, the lengths of the three transmission lines are $l(Z_1) = 1 \text{ km}$, $l(Z_2) = 2 \text{ km}$, and $l(Z_3) = 3 \text{ km}$, respectively.

Bode diagrams of the output impedance frequency responses of the three GCIs obtained by frequency scanning method are shown as the black dashed line labeled by 'Original FR' in Fig. 7(a). In addition, the Bode diagrams of the fitted transfer functions using VF algorithm with the order chosen as 1, 2, 3, 4, and 5 are also plotted. It can be seen that the fitting accuracy increases as the fitting order increases. The Bode diagrams in the non-passive frequency range (1423 Hz, 1667 Hz) are further plotted in Fig. 7(b), since the harmonic instability phenomena tend to occur in this frequency range [23]. It can be seen that the Bode diagrams of the original



(a)



(b)

Fig. 7. Bode diagrams of the terminal impedance frequency responses of the three GCIs in Fig. 6 and the fitted transfer functions using the VF algorithm with different orders. (a) Full view. (b) Zoomed view.

frequency responses and the fitted 5-order transfer function are highly overlapped, which indicates that the fitted 5-order transfer function is capable.

As defined in (14), the system LIM can be established at the four nodes in Fig. 6. For example, the system LIMs established at nodes #1, #2, and #3 can be derived as

$$Z_{iLIM} = (Z_{iLIM_1} // Z_{iLIM_2} + Z_i) // Z_{iS} \quad (39)$$

where $Z_{iLIM_1} = Z_g // (Z_{jS} + Z_j)$, $Z_{iLIM_2} = Z_{kS} + Z_k$, $i, j, k \in \{1, 2, 3\}$ and $i \neq j \neq k$.

In addition, the system LIM established at node #4 can be derived as

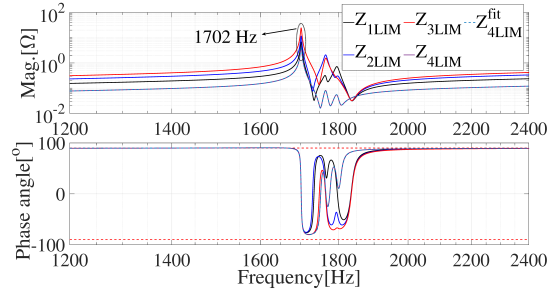
$$Z_{4LIM} = Z_{4LIM_1} // Z_{4LIM_2} \quad (40)$$

where $Z_{4LIM_1} = Z_g // (Z_{3S} + Z_3)$ and $Z_{4LIM_2} = (Z_{1S} + Z_1) // (Z_{2S} + Z_2)$.

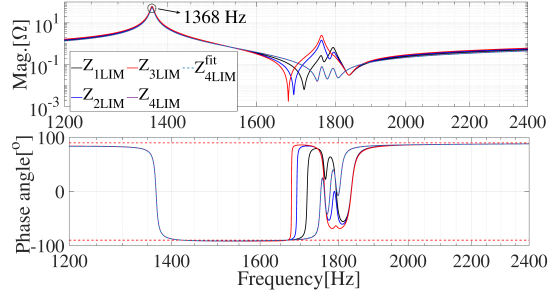
A. Stable Cases

Based on the measured impedance frequency responses of the three GCIs in Fig. 7, the Bode diagram of Z_{4LIM} when $l(Z_g)$ are 1 km and 13 km are calculated using (40), and plotted in Figs. 8(a) and 8(b), respectively. The fitted transfer functions of Z_{4LIM} using the VF algorithm with 16 order are shown as Z_{4LIM}^{fit} . It can be seen that the system LIM frequency responses can be accurately reproduced by the fitted 16-order transfer functions. In addition, both Z_{4LIM} and Z_{4LIM}^{fit} predict that the system has stable resonance frequencies 1702 Hz and 1368 Hz when $l(Z_g)$ are 1 km and 13 km, respectively, since the phase angles at the two resonance frequencies are within $[-90^\circ, 90^\circ]$ under the two cases.

The zeros of Z_{4LIM}^{fit} when $l(Z_g)$ are 1 km and 13 km are plotted in Fig. 9, which are $-8.985 \pm j10690$ and



(a)



(b)

Fig. 8. Bode diagrams of Z_{iLIM} ($i \in [1, 4]$) and the fitted transfer functions using the VF algorithm. (a) $l(Z_g) = 1$ km. (b) $l(Z_g) = 13$ km.

$-21.72 \pm j8596$, respectively. It indicates that the system is stable at $\frac{10690}{2\pi} = 1701$ Hz and $\frac{8596}{2\pi} = 1368$ Hz under the two cases, respectively, since the real parts of the zeros are negative. The identified zeros and corresponding stability analysis results highly agree with the Bode diagrams in Fig. 8, which validates the effectiveness of VF algorithm to extract the zeros information from LIM frequency responses. Since the system is assessed as stable under the two cases, no further component-level and parameter-level harmonic stability analysis are needed.

The Bode diagrams of the system LIMs calculated at nodes #1, #2, and #3 using (39) when $l(Z_g)$ are 1 km and 13 km are also plotted in Fig. 8. It can be seen from the four magnitude-frequency diagrams that the system LIMs calculated at the four nodes have the same resonance peak. Furthermore, the identified zeros of Z_{iLIM}^{fit} ($i \in [1, 3]$) using the VF algorithm are plotted in Fig. 9 (The fitting results of Z_{iLIM} ($i \in [1, 3]$) are not plotted in Fig. 8 for simplicity). It can be seen that the zeros of the four fitted transfer functions, i.e., Z_{iLIM}^{fit} ($i \in [1, 4]$), are the same, which indicates that the LIM derived at a certain node is able to obtain global stability analysis results. The correctness of the theoretical analysis in Section II-A is thus validated.

B. Unstable Cases

1) *Step 1. System-Level Harmonic Stability Analysis:* Based on the measured impedance frequency responses of the three GCIs in Fig. 7, the Bode diagrams of Z_{4LIM} when $l(Z_g)$ are 6 km and 8 km are calculated using (40), and plotted in Figs. 10(a) and 10(b), respectively. The fitted transfer functions of Z_{4LIM} using the VF algorithm with 16 order are shown as Z_{4LIM}^{fit} . It can be seen that the system LIM frequency

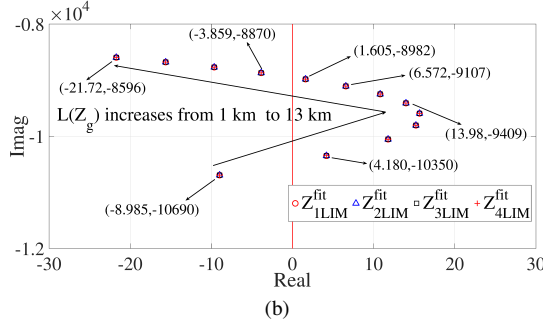
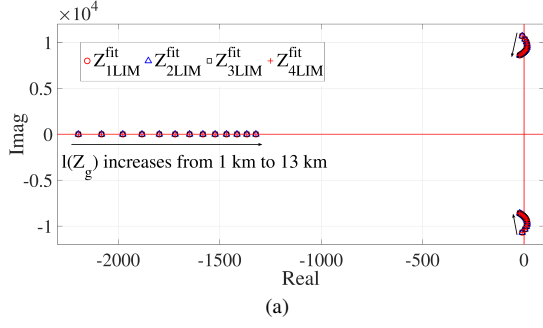


Fig. 9. Zeros trajectories of Z_{iLIM}^{fit} ($i \in [1, 4]$) when $1 \text{ km} < l(Z_g) < 13 \text{ km}$ (Step size: 1 km). (a) Full view. (b) Zoomed view.

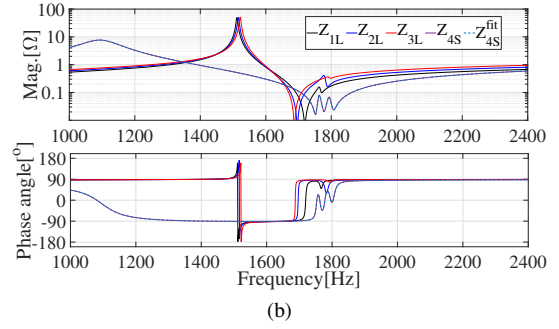
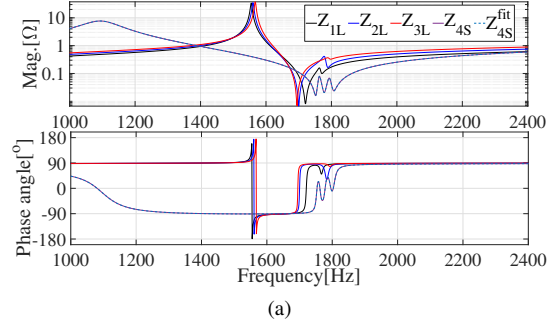


Fig. 11. Bode diagrams of the measured Z_{1L} , Z_{2L} , Z_{3L} , and Z_{4S} in Fig. 6 and the fitted results using the VF algorithm. (a) $l(Z_g) = 6 \text{ km}$. (b) $l(Z_g) = 8 \text{ km}$.

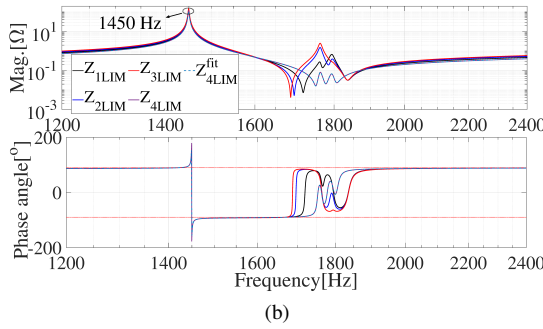
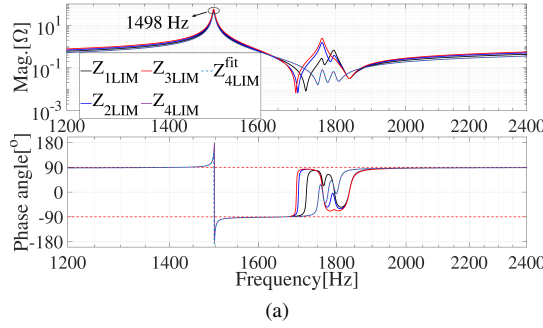


Fig. 10. Bode diagrams of Z_{iLIM} ($i \in [1, 4]$) and the fitted transfer functions using the VF algorithm. (a) $l(Z_g) = 6 \text{ km}$. (b) $l(Z_g) = 8 \text{ km}$.

responses can be accurately reproduced by the fitted 16-order transfer functions. In addition, both Z_{4LIM} and Z_{4LIM}^{fit} predict that the system has unstable resonance frequencies 1498 Hz and 1450 Hz when $l(Z_g)$ are 6 km and 8 km, respectively, since the phase angles at the two resonance frequencies are outside $[-90^\circ, 90^\circ]$ under the two cases.

The zeros of Z_{4LIM}^{fit} when $l(Z_g)$ are 6 km and 8 km are plotted in Fig. 9. It can be seen that the critical zeros of

Z_{4LIM}^{fit} when $l(Z_g)$ are 6 km and 8 km are $13.98 \pm j9409$ and $6.572 \pm j9107$, respectively, which indicates that the system is unstable at $\frac{9409}{2\pi} = 1498 \text{ Hz}$ and $\frac{9107}{2\pi} = 1449 \text{ Hz}$ under the two cases, respectively, since the real parts of the zeros are positive. The identified zeros and corresponding stability analysis results highly agree with the Bode diagrams in Fig. 10, which again validates the effectiveness of the VF algorithm to extract the zeros information from the LIM frequency responses. Since the system is assessed as unstable under the two cases, it's necessary to perform further component-level and parameter-level harmonic stability analysis.

The Bode diagrams of the system LIMs calculated at nodes #1, #2, and #3 using (39) and the identified zeros when $l(Z_g)$ are 6 km and 8 km are also plotted in Figs. 10 and 9, respectively (The fitted results of Z_{iLIM} ($i \in [1, 3]$) are not plotted in Fig. 10 for simplicity). It can be seen that the system is assessed as unstable regardless which node is selected to calculate the system LIM.

Besides the aforementioned four cases, i.e., $l(Z_g)$ are 1 km, 6 km, 8 km, and 13 km, the zeros trajectories of Z_{iLIM}^{fit} ($i \in [1, 4]$) when $l(Z_g)$ increases from 1 km to 13 km with step size 1 km are also plotted in Fig. 9. It can be seen that the zeros of the four LIMs are the same, and the system is assessed as globally stable when $l(Z_g) \in \{1 \text{ km}, 10 \text{ km}, 11 \text{ km}, 12 \text{ km}, 13 \text{ km}\}$ and globally unstable when $l(Z_g) \in \{2 \text{ km}, 3 \text{ km}, 4 \text{ km}, 5 \text{ km}, 6 \text{ km}, 7 \text{ km}, 8 \text{ km}, 9 \text{ km}\}$.

2) *Step 2. Component-Level Harmonic Stability Analysis:*
The NC can be performed at nodes #1, #2, #3, and #4 in Fig. 6. According to the components aggregation principles shown in Section II-A1, when the NC is performed at node # i ($i = 1, 2, 3$), the # i GCI is physically identified as the source part, and the rest of Fig. 6 is physically identified as the load

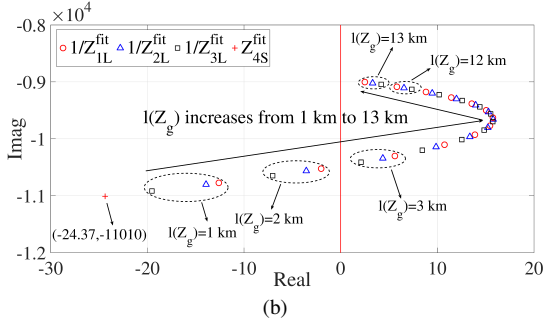
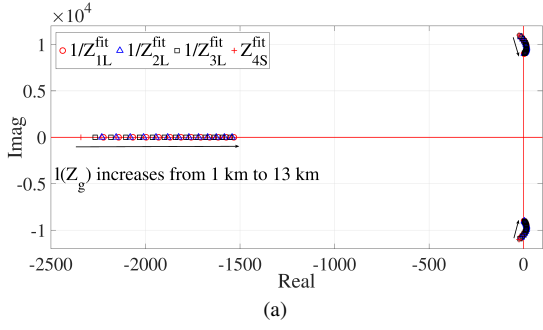


Fig. 12. Zeros trajectories of $1/Z_{1L}^{fit}$, $1/Z_{2L}^{fit}$, $1/Z_{3L}^{fit}$ and Z_{4S}^{fit} when $1 \text{ km} < l(Z_g) < 13 \text{ km}$ (Step size: 1 km). (a) Full view. (b) Zoomed view.

part. In addition, when the NC is performed at node #4, the grid is physically identified as the load part, and the rest of Fig. 6 is physically identified as the source part. The frequency responses of Z_{1L} , Z_{2L} , Z_{3L} , and Z_{4S} are calculated based on the impedance characteristics of the GCIs shown in Fig. 7. The derived Bode diagrams and corresponding fitted curves when $l(Z_g)$ are 6 km and 8 km are plotted in Fig. 11 (The fitted results of Z_{iL} ($i \in [1, 3]$) are not plotted in Fig. 11 for simplicity). On its basis, the zeros of $1/Z_{1L}^{fit}$, $1/Z_{2L}^{fit}$, $1/Z_{3L}^{fit}$, and Z_{4S}^{fit} are plotted in Fig. 12. It can be seen that Z_{4S}^{fit} does not have RHP zeros, whereas $1/Z_{1L}^{fit}$, $1/Z_{2L}^{fit}$, and $1/Z_{3L}^{fit}$ have RHP zeros, i.e., Z_{1L}^{fit} , Z_{2L}^{fit} , and Z_{3L}^{fit} have RHP poles, when $3 \text{ km} \leq l(Z_g) \leq 13 \text{ km}$. In addition, the Nyquist plots of the impedance ratios $\frac{Z_{iL}}{Z_{iS}}$ ($i \in [1, 4]$) when $l(Z_g)$ are 6 km and 8 km are plotted in Figs. 13(a) and 13(b), respectively. It can be seen that, under both cases, the Nyquist plots of $\frac{Z_{4L}}{Z_{4S}}$ encircle $-1 + j0$ in counterclockwise direction, whereas the Nyquist plots of $\frac{Z_{iL}}{Z_{iS}}$ ($i \in [1, 3]$) do not encircle $-1 + j0$. In addition, the Nyquist plots of the four impedance ratios when $l(Z_g)$ are 1 km and 13 km are plotted in Figs. 13(c) and 13(d), respectively. For clarity, the information is collected in Fig. 14. According to (8), the NC at all of the four nodes assesses that I_{iL} has two RHP poles when $l(Z_g)$ are 6 km and 8 km. In addition, the NC at all of the four nodes assesses that I_{iL} does not have any RHP poles when $l(Z_g)$ are 1 km and 13 km. The NC-based stability analysis results agree with the LIM-based stability analysis results in Fig. 9.

Since the Nyquist plot of $\frac{Z_{3L}}{Z_{3S}}$ is closest to $-1 + j0$ among $\frac{Z_{iL}}{Z_{iS}}$ ($i \in [1, 3]$) when $l(Z_g)$ are 6 km and 8 km, node #3 is identified as the weakest point among nodes #1, #2, and #3. The output impedance of the #3GCI should be reshaped to improve the stability at node #3.

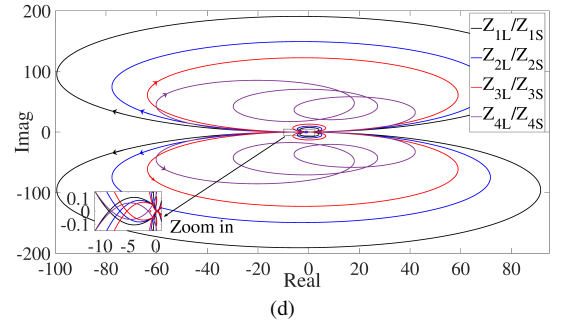
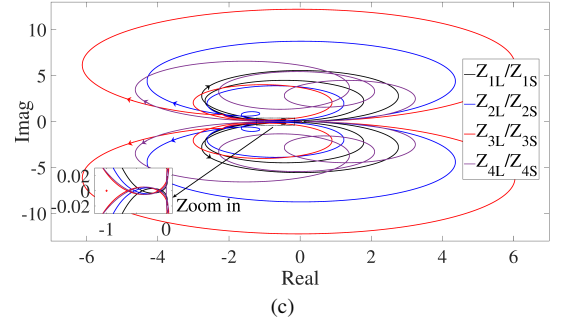
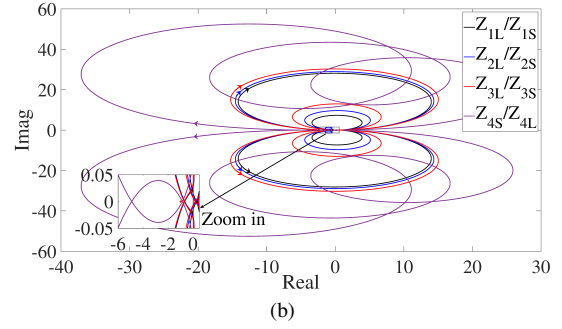
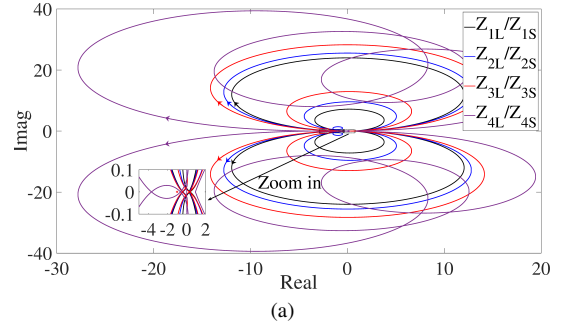


Fig. 13. Nyquist plots of the impedance ratios $\frac{Z_{iL}}{Z_{iS}}$ ($i \in [1, 4]$). (a) $l(Z_g) = 6 \text{ km}$. (b) $l(Z_g) = 8 \text{ km}$. (c) $l(Z_g) = 1 \text{ km}$. (d) $l(Z_g) = 13 \text{ km}$.

3) Step 3. Parameter-Level Harmonic Stability Analysis: Coefficients of the fitted 5-order transfer function in form of (17) of the impedance frequency responses of #3GCI in Fig. 7 are shown in Table I. According to (30), parameters of #3GCI can be identified as

$$L_{f2} = E = 0.2 \text{ mH} \quad K_p = \frac{B_0}{A_0} = 1.2 \Omega \quad (41)$$

By substituting $T_s = 10^{-4} \text{ s}$, $\omega_c = 2\pi 1546 \text{ rad/s}$, and (41) into (34) and (38), two equations which constraint L_{f1} , C_f ,

1 km	$P(Z_{il})$	$P(Y_{is})$	$N_{(-1,j0)}(Z_{il}Y_{is})$	$P(I_{il})$
Node #1	0	0	0	0
Node #2	0	0	0	0
Node #3	0	0	0	0
Node #4	0	0	0	0

(a)

6 km, 8 km	$P(Z_{il})$	$P(Y_{is})$	$N_{(-1,j0)}(Z_{il}Y_{is})$	$P(I_{il})$
Node #1	2	0	0	2
Node #2	2	0	0	2
Node #3	2	0	0	2
Node #4	0	0	2	2

(b)

13 km	$P(Z_{il})$	$P(Y_{is})$	$N_{(-1,j0)}(Z_{il}Y_{is})$	$P(I_{il})$
Node #1	2	0	2	0
Node #2	2	0	2	0
Node #3	2	0	2	0
Node #4	0	0	0	0

(c)

Fig. 14. Summary of the NC-based stability analysis results in Figs. 12 and 13. (a) $l(Z_g) = 1$ km. (b) $l(Z_g) = 6$ km and 8 km. (c) $l(Z_g) = 13$ km.

TABLE I
COEFFICIENTS OF THE FITTED 5-ORDER TRANSFER FUNCTION IN FORM OF (17)

A_5	A_4	A_3	A_2	A_1	A_0
1	7.4861e4	4.2703e9	6.6168e13	2.4013e17	2.8359e21
B_5	B_4	B_3	B_2	B_1	B_0
-0.0578	2.2403e4	1.2844e9	9.1900e13	1.0928e18	3.4030e21
E	2.0025e-4				

and K_{cp} can be obtained, which can further be simplified as

$$f(C_f, K_{cp}) = 0 \quad (42)$$

where the detailed expression is omitted for simplicity. Since the solution space has one freedom, the accurate solution can be found in a trial-and-error way. For example, different values of C_f can be first assumed, and the value of C_f which makes the calculated Bode diagram agree with the measured terminal impedance frequency responses is then selected, as shown in Fig. 15. Fig. 16 shows frequency responses of the calculated terminal impedance formulas with different C_f . It can be seen that the calculated frequency response agrees with the original terminal impedance frequency response when $C_f = 50 \mu\text{F}$ and $K_{cp} = 0.6 \Omega$. The identified circuit and controller parameters of the #3GCI are listed as follows. $L_{f1} = 0.5$ mH, $L_{f2} = 0.2$ mH, $C_f = 50 \mu\text{F}$, $K_p = 1.2 \Omega$, and $K_{cp} = 0.6 \Omega$.

System stability can then be improved by re-tuning the identified controller parameters. Zeros of Z_{ALIM} by re-tuning the capacitor-current proportional feedback active damping coefficient K_{cp} of #1GCI or #3GCI under the two unstable cases are summarized in Table II, where \mathbf{K}_{cpi} ($i \in [1, 5]$) are the collections of K_{cp} of the three GCIs. In detail, $\mathbf{K}_{cp1} = \{0.60\Omega, 0.60\Omega, 0.60\Omega\}$, $\mathbf{K}_{cp2} = \{0.60\Omega, 0.60\Omega, 0.85\Omega\}$, $\mathbf{K}_{cp3} = \{0.85\Omega, 0.60\Omega, 0.60\Omega\}$, $\mathbf{K}_{cp4} = \{0.60\Omega, 0.60\Omega, 0.68\Omega\}$, and $\mathbf{K}_{cp5} = \{0.68\Omega, 0.60\Omega, 0.60\Omega\}$. When $l(Z_g)$ is 6 km,

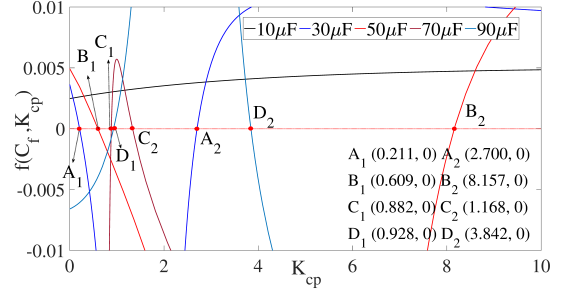
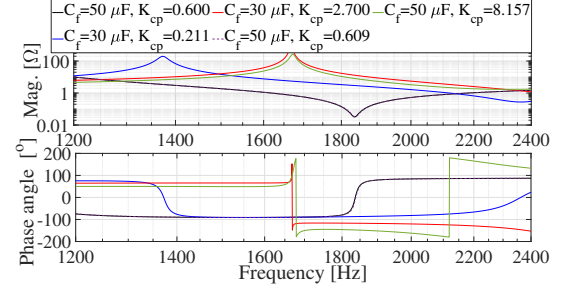
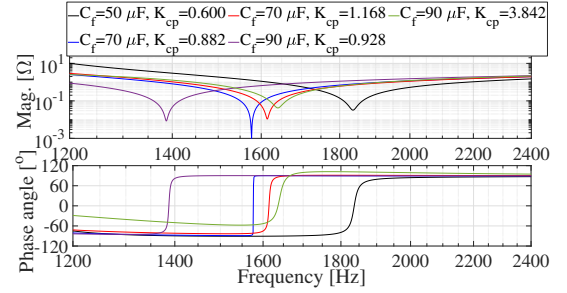


Fig. 15. Waveforms of $f(C_f, K_{cp})$ with different values C_f .



(a)



(b)

Fig. 16. Bode diagrams of the impedance frequency responses calculated by (25) with different C_f .

if K_{cp} of #3GCI is increased from 0.60Ω to 0.85Ω , the critical zeros of Z_{ALIM} are changed from $13.98 \pm j9409$ to $-1.643 \pm j9505$, which indicates that the system is stabilized. However, if K_{cp} of #1GCI is increased from 0.60Ω to 0.85Ω , the critical zeros of Z_{ALIM} are changed from $13.98 \pm j9409$ to $1.222 \pm j9486$, which indicates that the system is still unstable.

TABLE II
ZEROS OF Z_{ALIM} BY RE-TUNING K_{cp} OF #1GCI OR #3GCI

	$l(Z_g) = 6$ km			$l(Z_g) = 8$ km			
\mathbf{K}_{cp1}	13.98	$\pm j9409$	-1720	\mathbf{K}_{cp1}	6.572	$\pm j9107$	-1583
\mathbf{K}_{cp2}	-1.643	$\pm j9505$	-1730	\mathbf{K}_{cp4}	-0.7802	$\pm j9139$	-1586
\mathbf{K}_{cp3}	1.222	$\pm j9486$	-1728	\mathbf{K}_{cp5}	0.3261	$\pm j9134$	-1585

Similarly, when $l(Z_g)$ is 8 km, if K_{cp} of #3GCI is increased from 0.60Ω to 0.68Ω , the critical zeros of Z_{ALIM} are changed from $6.572 \pm j9107$ to $-0.7802 \pm j9139$, which indicates that the system is stabilized. However, if K_{cp} of #1GCI is increased from 0.60Ω to 0.68Ω , the critical zeros of Z_{ALIM} are changed from $6.572 \pm j9107$ to $0.3261 \pm j9134$, which indicates that the system is still unstable. The zeros analysis results of Z_{ALIM}

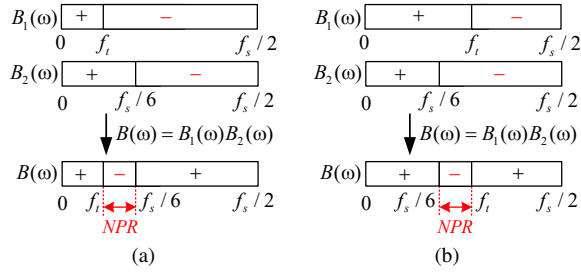


Fig. 17. The signs of $B_1(\omega)$, $B_2(\omega)$, and $B(\omega)$ up to the Nyquist frequency. (a) $f_t < f_s/6$. (b) $f_t > f_s/6$.

validate the correctness of the weakest point identifications in step 2.

On the other hand, the frequency-domain passivity theory offers another solution to enforce the system stability [40], [41], [56]. The core idea is to make the output impedances of all GCIs have non-negative real parts up to the Nyquist frequency, i.e., $\forall \omega \in [0, \frac{f_s}{2}]$, $real\{Z_{GCI}(\omega)\} \geq 0$. Therefore, the phase angle of $Z_{GCI}(\omega)$ can be limited within $[-90^\circ, 90^\circ]$ [40]. Taking the real part of (35) yields

$$real\{Z_{GCI}(\omega)\} = \frac{B(\omega)}{A(\omega)} \quad (43)$$

Since $A(\omega) > 0$, the sign of $real\{Z_{GCI}(\omega)\}$ is dependent on $B(\omega)$, which can be reformulated as

$$B(\omega) = B_1(\omega)B_2(\omega) \quad (44)$$

where

$$\begin{aligned} B_1(\omega) &= (K_{cp} - K_p)C_f L_{f1} \omega^2 + K_p \\ B_2(\omega) &= \cos(1.5\omega T_s) \end{aligned} \quad (45)$$

$B_2(\omega)$ changes the sign from positive to negative at $f_s/6$. Assume that f_t is the frequency point where $B_1(\omega)$ changes the sign from positive to negative, which can be calculated as

$$f_t = \sqrt{\frac{K_p}{4\pi^2(K_p - K_{cp})C_f L_{f1}}} \quad (46)$$

Then, the signs of $B_1(\omega)$, $B_2(\omega)$, and $B(\omega)$ up to the Nyquist frequency can be summarized in Fig. 17. It can be seen that when $f_t < f_s/6$, $(f_t, f_s/6)$ is the non-passivity region (NPR) of $B(\omega)$. In addition, when $f_t > f_s/6$, $(f_s/6, f_t)$ is the NPR of $B(\omega)$. Therefore, in order to eliminate the NPR of $B(\omega)$, f_t should be equal to $f_s/6$, i.e.,

$$f_t = \frac{f_s}{6} \Rightarrow K_{cp} = K_p - \frac{9K_p}{\pi^2 f_s^2 C_f L_{f1}} \quad (47)$$

By substituting the identified circuit and controller parameters of the GCIs into (47), K_{cp} is calculated as 0.76. The phase angle of the terminal impedance frequency responses of the three GCIs after passivity enforcement is shown in Fig. 18. It can be seen that, the NPR (1423 Hz, 1667 Hz) in Fig. 7 disappears by increasing K_{cp} from 0.60 to 0.76.

Obviously, the frequency-domain passivity enforcement solution is more robust than the aforementioned capacitor-current

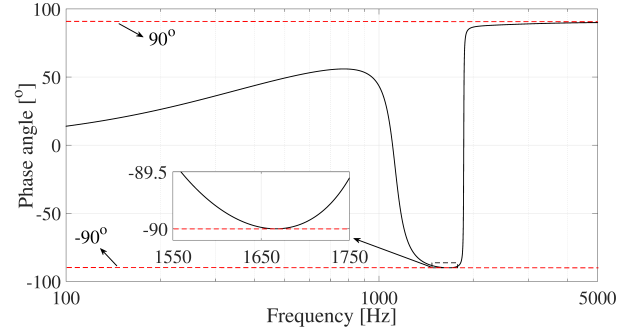


Fig. 18. Phase angle of the terminal impedance frequency responses of the three GCIs in Fig. 6 after passivity enforcement.

feedback coefficient re-tuning method, since the interconnected passive system can be guaranteed to be stable when arbitrary system changes happen [41]. In fact, the passivity theory provides a sufficient yet not necessary stability condition for the interconnected system, i.e., it is a little conservative. For example, as shown in Table II, the unstable system when $l(Z_g)$ is 8 km can be stabilized by only increasing K_{cp} of #3GCI from 0.60 Ω to 0.68 Ω , instead of enforcing system passivity by increasing K_{cp} of all of the three GCIs from 0.60 to 0.76. Besides, re-tuning K_{cp} of only one GCI in step 3 has an additional purpose, i.e., to validate the correctness of the weakest point identification results in step 2.

C. Extension of the Proposed Method for Low-Frequency Instability Source Identification

In addition to the inner current control loop-induced high-frequency harmonic instability phenomena shown in Sections IV-B, low-frequency instability phenomena may also happen, which commonly result from slower outer control loops, e.g., PLL [8], outer power control loop [9], and dc-link voltage control loop [11]. Different from only considering the inner current control loop which can be depicted by the phasor-domain impedance model in (25), 2×2 impedance matrices should be established to reveal asymmetric characteristics of d-axis and q-axis control of these outer control loops [8], [9], [11], [57]. To cope with the two-dimensional impedance models, the gray-box hierarchical instability source identification method presented in Section III should be slightly modified. In step 1, since the LIM derived at a specific node using the basic circuit laws is now a two-dimensional matrix, the system stability should be assessed by the zeros of the determinant of the LIM [36]. If the real parts of all zeros are negative, the system is globally stable. Otherwise, it is unstable. In step 2, the generalized NC should be used to the ratio of the two-dimensional impedance matrices of the source and load parts [8].

In step 3, the circuit and controller parameters of the GCI under other control strategies, e.g., converter-side current control and capacitor-voltage derivative feedback active damping, can also be identified. The circuit and controller parameters of the GCI under converter-side current control or grid-side current control without active damping are identified in [55]. In addition, the capacitor-voltage derivative feedback

active damping is equivalent to the capacitor-current proportional feedback active damping from the perspective of output impedance model [54], i.e., the identification algorithm is the same as the method presented in this paper. Furthermore, when the outer control loops are further considered, only a few modifications should be made. Similar with (25), the two-dimensional impedance matrices are first theoretically derived. Then, a two-dimensional transfer function matrix is fitted from the measured two-dimensional impedance frequency responses using the enhanced version of the VF algorithm, i.e., the matrix fitting (MF) algorithm, and is equalized with the theoretically-derived one. On its basis, the controller parameters of outer control loops can further be identified. For example, the parameters of current controller, dc voltage controller, and the PLL are identified in [16].

V. REAL-TIME SIMULATION VERIFICATION

In this section, the correctness of the harmonic stability analysis results in Section IV obtained by the proposed gray-box hierarchical instability source identification method is validated by both simulation results in Matlab/Simulink platform and real-time verification results in OPAL-RT digital simulator platform.

A. Simulation Verification Based on Matlab/Simulink Platform

System parameters of the three GCIs in Fig. 6 are shown in Table III. It can be seen that the identified circuit and controller parameters of the GCI in Section IV-B3 highly agree with actual circuit and controller parameters.

TABLE III
SYSTEM PARAMETERS OF THE THREE GCIS IN FIG. 6

Parameter	Value
DC-link voltage V_{dc}	1150 V
Grid fundamental angular frequency ω_1	50 Hz
Inverter-side filter inductance L_{f1}	0.5 mH
Grid-side filter inductance L_{f2}	0.2 mH
Filter capacitance C_f	50 μ F
Capacitor-current-feedback coefficient K_{cp}	0.6 Ω
Switching frequency f_{sw}	2.5 kHz
Sampling frequency f_s	10 kHz
Grid voltage (phase-to-phase RMS) V_g	575 V
Proportional gain of current controller K_p	1.2 Ω
Integral gain of current controller K_i	65 Ω /s
Proportional gain of PLL K_{pll}	0.7 rad/(Vs)
Integral gain of PLL K_{ipll}	3.2 rad/(Vs ²)
Current reference value $I_{g,d}^{ref}$	1.0 kA
Current reference value $I_{g,q}^{ref}$	0 A

1) *Stable Cases:* Time-domain simulation results of grid current I_g when $l(Z_g) = 1$ km and $l(Z_g) = 13$ km are shown in Fig. 19(a) before 0.5 s and in Fig. 20(a) before 0.5 s, respectively. It can be seen that the grid currents under the two cases are stable, which agree with the stability analysis results in Section IV-A.

2) *Unstable Cases:* Time-domain simulation results of grid current I_g when $l(Z_g) = 6$ km and $l(Z_g) = 8$ km are shown in Fig. 19(a) from 0.5 s to 1.5 s and in Fig. 20(a) from 0.5 s to 1.5 s, respectively. It can be seen that the grid currents under the

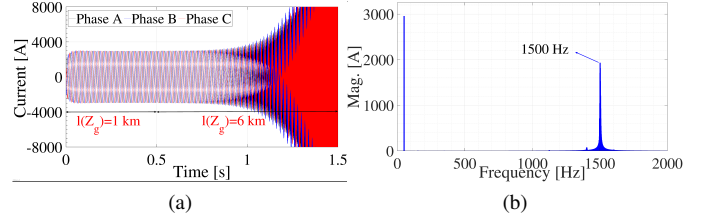


Fig. 19. Simulation results of grid current I_g when $l(Z_g)$ increases from 1 km to 6 km at 0.5 s. (a) Time-domain waveform of I_g . (b) FFT of I_g after 0.5 s.

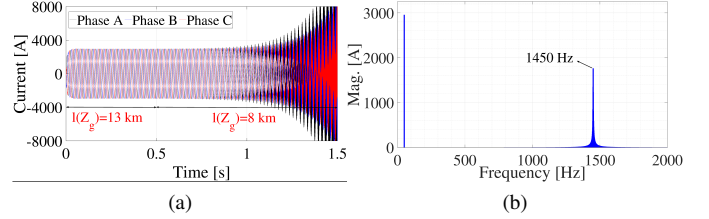


Fig. 20. Simulation results of grid current I_g when $l(Z_g)$ decreases from 13 km to 8 km at 0.5 s. (a) Time-domain waveform of I_g . (b) FFT of I_g after 0.5 s.

two cases are unstable, which agree with the stability analysis results in Section IV-B. In addition, the frequency spectrums of I_g under the two unstable cases are shown in Figs. 19(b) and 20(b), respectively. It can be seen that harmonic instability occurring at 1500 Hz when $l(Z_g) = 6$ km oscillates faster than that occurring at 1450 Hz when $l(Z_g) = 8$ km, which agree with the identified RHP zeros $13.98 \pm j2\pi 1497.5$ and $6.572 \pm j2\pi 1449.4$ in Fig. 9. The correctness of the harmonic stability analysis results in Section IV-B is thus validated.

Furthermore, the system becomes stable by increasing K_{cp} of the #3GCI from 0.6 Ω to 0.85 Ω at 1.2 s when $l(Z_g) = 6$ km, and from 0.6 Ω to 0.68 Ω at 1.2 s when $l(Z_g) = 8$ km, respectively, as shown in Fig. 21, which agree with the theoretical analysis results in Section IV-B.

B. Real-Time Verification Based on OPAL-RT Digital Simulator Platform

Real-time simulation verification based on OPAL-RT digital simulator platform is performed to further validate the correctness of the theoretical analysis results in Section IV and the time-domain simulation results obtained in Matlab/Simulink

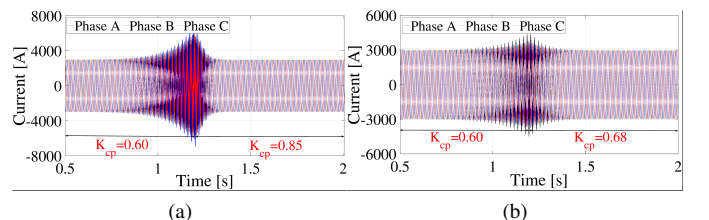


Fig. 21. Simulation results of grid current I_g with re-tuning K_{cp} at 1.2 s. (a) K_{cp} re-tuned from 0.6 Ω to 0.85 Ω when $l(Z_g) = 6$ km. (b) K_{cp} re-tuned from 0.6 Ω to 0.68 Ω when $l(Z_g) = 8$ km.



Fig. 22. Configuration of the OPAL-RT digital simulator setup.

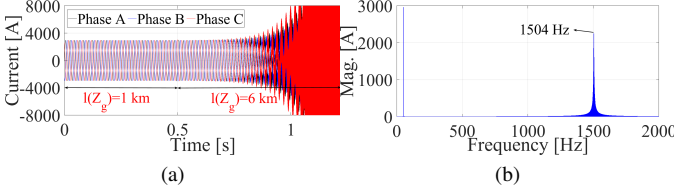


Fig. 23. Real-time verification of the Matlab/Simulink-based simulation results in Fig. 19. (a) Time-domain waveform of I_g . (b) FFT of I_g after 0.5 s.

platform. Fig. 22 shows configuration of the OPAL-RT digital simulator platform. The OP5600 combines the power and reliability of Intel Xeon E5 processing cores with the high-performance latest generation Xilinx Virtex-6 FPGA to address a wide range of rapid control prototyping applications with OPAL-RT's RT-LAB or HYPERSIM software platforms. The Simulink-based model is established in the RT-LAB software, based on which code is generated and downloaded into the OP5600 hardware. Both software and hardware platforms allow high-speed and real-time simulation. The real-time simulation results obtained by OPAL-RT platform are then processed in Matlab.

1) *Stable Cases*: The OPAL-RT-based real-time verification of the Matlab/Simulink-based simulation results when $l(Z_g) = 1$ km and $l(Z_g) = 13$ km are shown in Fig. 23 before 0.5 s and in Fig. 24 before 0.5 s, respectively. It can be seen that the real-time simulation results before 0.5 s are stable, which agree with the theoretical analysis results in Section IV-A and the Matlab/Simulink-based simulation results in Figs. 19 and 20 before 0.5 s.

2) *Unstable Cases*: The OPAL-RT-based real-time verification of the Matlab/Simulink-based simulation results when $l(Z_g) = 6$ km and $l(Z_g) = 8$ km are shown in Fig. 23(a) after 0.5 s and in Fig. 24(a) after 0.5 s, respectively. It can be seen that, under the two cases, the real-time simulation results are unstable, which agree with the theoretical analysis results in Section IV-A and the Matlab/Simulink-based simulation results in Figs. 19(a) and 20(a) from 0.5 s to 1.5 s. In addition, the frequency spectrums of I_g under the two unstable cases are shown in Figs. 23(b) and 24(b), respectively. It can be seen that harmonic instability occurring at 1504 Hz when $l(Z_g) = 6$ km oscillates faster than that occurring at 1451 Hz when $l(Z_g) = 8$ km, which highly agree with the FFT analysis results in Figs. 19(b) and 20(b).

Fig. 25 shows the real-time simulation results when K_{cp} is changed. It can be seen that the system becomes stable by

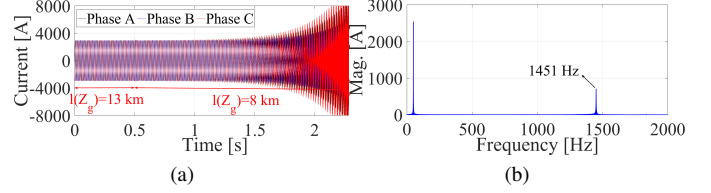


Fig. 24. Real-time verification of the Matlab/Simulink-based simulation results in Fig. 20. (a) Time-domain waveform of I_g . (b) FFT of I_g after 0.5 s.

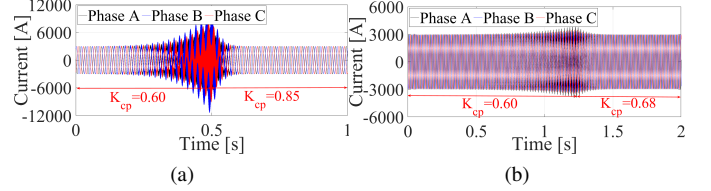


Fig. 25. Real-time verification of the Matlab/Simulink-based simulation results in Fig. 21. (a) K_{cp} re-tuned from 0.60 Ω to 0.85 Ω when $l(Z_g) = 6$ km. (b) K_{cp} re-tuned from 0.60 Ω to 0.68 Ω when $l(Z_g) = 8$ km.

increasing K_{cp} from 0.60 Ω to 0.85 Ω when $l(Z_g) = 6$ km, and becomes stable by increasing K_{cp} from 0.60 Ω to 0.68 Ω when $l(Z_g) = 8$ km, which agree with the Matlab/Simulink-based simulation results in Fig. 21.

VI. CONCLUSION

This paper presents a gray-box hierarchical instability source identification method for multi-inverter-fed power systems, which is able to perform stability assessment at system, component, and parameter levels sequentially based on measured output impedance frequency responses of the GCIs. The proposed method improves the conventional eigenvalues-based and impedance-based stability analysis methods by extracting eigenvalues information from the impedance frequency responses. On system level, the system eigenvalues are identified from the system LIM which is derived by applying the basic circuit principles to the component impedances. On component level, RHP poles of impedance ratio calculated for the NC are identified with the help of the VF algorithm. On parameter level, critical circuit and controller parameters of the problematic GCIs are identified from the fitted output impedance transfer functions. Theoretical analysis, simulation, and real-time verification results show that the proposed method can identify the instability phenomena and corresponding oscillation frequency, based on which the problematic components and controller parameters can further be located. The proposed method is able to perform up-down stability analysis and controller re-tuning for stability improvement even if no internal parameters are provided. Low-frequency instability phenomena induced by other control loops, e.g., PLL, dc-link voltage control loop, and outer power control loop, will be investigated using the proposed method in future works.

APPENDIX A

PROOF OF RELATION AMONG EIGENVALUES-BASED,
NC-BASED, AND LIM-BASED STABILITY ANALYSIS
METHODS

(12) can be reformulated as

$$\begin{vmatrix} sI_p - A_{sys}^{11} & -A_{sys}^{12} \\ -A_{sys}^{21} & sI_q - A_{sys}^{22} \end{vmatrix} = 0 \rightarrow \Delta_1 \Delta_2 \Delta_3 = 0 \quad (48)$$

where

$$\begin{aligned} \Delta_1 &= |sI_p - A_{sys}^{11}| \\ \Delta_2 &= |sI_q - A_{sys}^{22}| \\ \Delta_3 &= \left| I_q - (sI_q - A_{sys}^{22})^{-1} A_{sys}^{21} (sI_p - A_{sys}^{11})^{-1} A_{sys}^{12} \right| \end{aligned} \quad (49)$$

Based on (11), Δ_1 can be reformulated as

$$\Delta_1 = |sI_p - A_{iS}| |\Lambda_1| \quad (50)$$

where

$$\begin{aligned} |sI_p - A_{iS}| &= \prod_{m=1}^p (s - \lambda_{iSx}) \\ \Lambda_1 &= I_p + (sI_p - A_{iS})^{-1} B_{iS} (1 + D_{iL} D_{iS})^{-1} D_{iL} C_{iS} \end{aligned} \quad (51)$$

Furthermore, $|\Lambda_1|$ can be reformulated as

$$|\Lambda_1| = \left| I_p + C_{iS}^{-1} C_{iS} (sI_p - A_{iS})^{-1} B_{iS} (1 + D_{iL} D_{iS})^{-1} D_{iL} C_{iS} \right| \quad (52)$$

According to (3), $C_{iS} (sI_p - A_{iS})^{-1} B_{iS} = Y_{iS} - D_{iS}$. Therefore, (52) can be reformulated as

$$|\Lambda_1| = \left(\frac{1 + D_{iL} Y_{iS}}{1 + D_{iL} D_{iS}} \right)^p \quad (53)$$

Similarly, based on (11), Δ_2 can be reformulated as

$$\Delta_2 = |sI_q - A_{iL}| |\Lambda_2| \quad (54)$$

where

$$\begin{aligned} |sI_q - A_{iL}| &= \prod_{y=1}^q (s - \lambda_{iLy}) \\ \Lambda_2 &= I_q + (sI_q - A_{iL})^{-1} B_{iL} (1 + D_{iL} D_{iS})^{-1} D_{iS} C_{iL} \\ |\Lambda_2| &= \left(\frac{1 + D_{iS} Z_{iL}}{1 + D_{iL} D_{iS}} \right)^q \end{aligned} \quad (55)$$

In addition, based on (11), Δ_3 can be reformulated as

$$\begin{aligned} \Delta_3 &= (1 + (Z_{iL} - D_{iL})(Y_{iS} - D_{iS})(1 + D_{iL} D_{iS})^{-2}) |\Lambda_1|^{-\frac{1}{p}} \\ &\quad \dots |\Lambda_2|^{-\frac{1}{q}} \end{aligned} \quad (56)$$

By substituting (53) and (55) into (56), (56) can be simplified as

$$\Delta_3 = \left(\frac{(1 + D_{iL} D_{iS})(1 + Z_{iL} Y_{iS})}{(1 + D_{iL} Y_{iS})(1 + D_{iS} Z_{iL})} \right)^q \quad (57)$$

Therefore, by substituting (49)-(57) into (48), (48) can be reformulated as

$$\begin{aligned} \Delta_1 \Delta_2 \Delta_3 &= \prod_{x=1}^p (s - \lambda_{iSx}) \prod_{y=1}^q (s - \lambda_{iLy}) \frac{(1 + D_{iL} Y_{iS})^{p-q}}{(1 + D_{iL} D_{iS})^p} \dots \\ &\quad (1 + Z_{iL} Y_{iS})^q = 0 \end{aligned} \quad (58)$$

APPENDIX B

DETAILED EXPRESSION OF $Z_{GCI}(\omega)$

$$\begin{aligned} Z_{GCI}(\omega) &= ((K_p - K_{cp} L_{f2} C_f \omega^2) \cos(1.5\omega T_s) - j(L_{f1} \dots \\ &\quad L_{f2} C_f \omega^3 - (L_{f1} + L_{f2})\omega + (K_p - K_{cp} C_f L_{f2} \omega^2) \dots \\ &\quad \sin(1.5\omega T_s)) / (1 - L_{f1} C_f \omega^2 + K_{cp} C_f \omega \sin(1.5\omega T_s) \dots \\ &\quad + jK_{cp} C_f \omega \cos(1.5\omega T_s)) \end{aligned} \quad (59)$$

REFERENCES

- [1] W. Zhou, Y. Wang, P. Cai, and Z. Chen, "A gray-box impedance reshaping method of grid-connected inverter for resonance damping," in *Proc. IEEE 2019 10th International Conference on Power Electronics and ECCE Asia (ICPE 2019-ECCE Asia)*, pp. 2660–2667.
- [2] Z. Chen, J. M. Guerrero, and F. Blaabjerg, "A review of the state of the art of power electronics for wind turbines," *IEEE Trans. Power Electron.*, vol. 24, no. 8, pp. 1859–1875, Aug. 2009.
- [3] S. Kouro, J. I. Leon, D. Vinnikov, and L. G. Franquelo, "Grid-connected photovoltaic systems: An overview of recent research and emerging PV converter technology," *IEEE Ind. Electron. Mag.*, vol. 9, no. 1, pp. 47–61, Mar. 2015.
- [4] "Renewables 2019 global status report," <https://www.ren21.net>, accessed: 2020-03-31.
- [5] "Global wind report," <http://www.gwec.net>, accessed: 2020-03-31.
- [6] F. Blaabjerg, Z. Chen, and S. B. Kjaer, "Power electronics as efficient interface in dispersed power generation systems," *IEEE Trans. Power Electron.*, vol. 19, no. 5, pp. 1184–1194, Sep. 2004.
- [7] X. Wang and F. Blaabjerg, "Harmonic stability in power electronic-based power systems: Concept, modeling, and analysis," *IEEE Trans. Smart Grid*, vol. 10, no. 3, pp. 2858–2870, May 2019.
- [8] B. Wen, D. Boroyevich, R. Burgos, P. Mattavelli, and Z. Shen, "Analysis of DQ small-signal impedance of grid-tied inverters," *IEEE Trans. Power Electron.*, vol. 31, no. 1, pp. 675–687, Jan. 2016.
- [9] W. Zhou, Y. Wang, R. E. Torres-Olguin, and Z. Chen, "Effect of reactive power characteristic of offshore wind power plant on low-frequency stability," *IEEE Trans. Energy Convers.*, Early Access, doi: 10.1109/TEC.2020.2965017.
- [10] W. Zhou, Y. Wang, D. Liu, and Z. Chen, "Optimization of active and reactive power dispatch among multi-paralleled grid-connected inverters considering low-frequency stability," in *Proc. IEEE 2019 45th Annual Conference of the IEEE Industrial Electronics Society (IES)*, pp. 6024–6031.
- [11] D. Lu, X. Wang, and F. Blaabjerg, "Impedance-based analysis of DC-link voltage dynamics in voltage-source converters," *IEEE Trans. Power Electron.*, vol. 34, no. 4, pp. 3973–3985, Apr. 2019.
- [12] D. Dong, B. Wen, D. Boroyevich, P. Mattavelli, and Y. Xue, "Analysis of phase-locked loop low-frequency stability in three-phase grid-connected power converters considering impedance interactions," *IEEE Trans. Ind. Electron.*, vol. 62, no. 1, pp. 310–321, Jan. 2015.
- [13] J. L. Agorreta, M. Borrega, J. Lopez, and L. Marroyo, "Modeling and control of N-paralleled grid-connected inverters with LCL filter coupled due to grid impedance in PV plants," *IEEE Trans. Power Electron.*, vol. 26, no. 3, pp. 770–785, Mar. 2011.
- [14] W. Zhou, Y. Wang, and Z. Chen, "Impedance-decoupled modeling method of multi-port transmission network in inverter-fed power plant," *IEEE Trans. Ind. Appl.*, vol. 56, no. 1, pp. 611–621, Jan./Feb. 2020.
- [15] D. Yang, X. Wang, and F. Blaabjerg, "Sideband harmonic instability of paralleled inverters with asynchronous carriers," *IEEE Trans. Power Electron.*, vol. 33, no. 6, pp. 4571–4577, Jun. 2018.
- [16] M. Amin and M. Molinas, "A gray-box method for stability and controller parameter estimation in HVDC-connected wind farms based on nonparametric impedance," *IEEE Trans. Ind. Electron.*, vol. 66, no. 3, pp. 1872–1882, Mar. 2019.
- [17] E. A. A. Coelho, P. C. Cortizo, and P. F. D. Garcia, "Small-signal stability for parallel-connected inverters in stand-alone AC supply systems," *IEEE Trans. Ind. Appl.*, vol. 38, no. 2, pp. 533–542, Mar./Apr. 2002.
- [18] N. Pogaku, M. Prodanovic, and T. C. Green, "Modeling, analysis and testing of autonomous operation of an inverter-based microgrid," *IEEE Trans. Power Electron.*, vol. 22, no. 2, pp. 613–625, Mar. 2007.

- [19] M. Rasheduzzaman, J. A. Mueller, and J. W. Kimball, "An accurate small-signal model of inverter-dominated islanded microgrids using dq reference frame," *IEEE J. Emerg. Sel. Top. Power Electron.*, vol. 2, no. 4, pp. 1070–1080, Dec. 2014.
- [20] Y. Wang, X. Wang, F. Blaabjerg, and Z. Chen, "Harmonic instability assessment using state-space modeling and participation analysis in inverter-fed power systems," *IEEE Trans. Ind. Electron.*, vol. 64, no. 1, pp. 806–816, Jan. 2017.
- [21] —, "Small-signal stability analysis of inverter-fed power systems using component connection method," *IEEE Trans. Smart Grid*, vol. 9, no. 5, pp. 5301–5310, Sep. 2018.
- [22] J. Sun, "Impedance-based stability criterion for grid-connected inverters," *IEEE Trans. Power Electron.*, vol. 26, no. 11, p. 3075, Nov. 2011.
- [23] C. Yoon, H. Bai, R. N. Beres, X. Wang, C. L. Bak, and F. Blaabjerg, "Harmonic stability assessment for multiparalleled, grid-connected inverters," *IEEE Trans. Sustain. Energy*, vol. 7, no. 4, pp. 1388–1397, Oct. 2016.
- [24] H. Bai, X. Wang, and F. Blaabjerg, "Passivity enhancement in renewable energy source based power plant with paralleled grid-connected VSIs," *IEEE Trans. Ind. Appl.*, vol. 53, no. 4, pp. 3793–3802, Jul./Aug. 2017.
- [25] X. Zhang, H. S.-h. Chung, L. L. Cao, J. P. W. Chow, and W. Wu, "Impedance-based stability criterion for multiple offshore inverters connected in parallel with long cables," in *Proc. IEEE 2017 Energy Conversion Congress and Exposition (ECCE)*, pp. 3383–3389.
- [26] H. Liu, X. Xie, C. Zhang, Y. Li, H. Liu, and Y. Hu, "Quantitative SSR analysis of series-compensated DFIG-based wind farms using aggregated RLC circuit model," *IEEE Trans. Power Syst.*, vol. 32, no. 1, pp. 474–483, Jan. 2017.
- [27] W. Cao, Y. Ma, and F. Wang, "Sequence-impedance-based harmonic stability analysis and controller parameter design of three-phase inverter-based multibus ac power systems," *IEEE Trans. Power Electron.*, vol. 32, no. 10, pp. 7674–7693, Oct. 2017.
- [28] W. Cao, Y. Ma, L. Yang, F. Wang, and L. M. Tolbert, "D-Q impedance based stability analysis and parameter design of three-phase inverter-based AC power systems," *IEEE Trans. Ind. Electron.*, vol. 64, no. 7, pp. 6017–6028, Jul. 2017.
- [29] E. Ebrahimzadeh, F. Blaabjerg, X. Wang, and C. L. Bak, "Harmonic stability and resonance analysis in large PMSG-based wind power plants," *IEEE Trans. Sustain. Energy*, vol. 9, no. 1, pp. 12–23, Jan. 2018.
- [30] —, "Reducing harmonic instability and resonance problems in PMSG-based wind farms," *IEEE J. Emerg. Sel. Top. Power Electron.*, vol. 6, no. 1, pp. 73–83, Mar. 2018.
- [31] —, "Bus participation factor analysis for harmonic instability in power electronics based power systems," *IEEE Trans. Power Electron.*, vol. 33, no. 12, pp. 10341–10351, Dec. 2018.
- [32] Y. Zhan, X. Xie, H. Liu, H. Liu, and Y. Li, "Frequency-domain modal analysis of the oscillatory stability of power systems with high-penetration renewables," *IEEE Trans. Sustain. Energy*, vol. 10, no. 3, pp. 1534–1543, Jul. 2019.
- [33] C. Zhang, M. Molinas, A. Rygg, and X. Cai, "Impedance-based analysis of interconnected power electronics systems: Impedance network modeling and comparative studies of stability criteria," *IEEE J. Emerg. Sel. Top. Power Electron.*, Early Access, doi: 10.1109/JESTPE.2019.2914560.
- [34] T. Roinila, T. Messo, and E. Santi, "MIMO-identification techniques for rapid impedance-based stability assessment of three-phase systems in DQ domain," *IEEE Trans. Power Electron.*, vol. 33, no. 5, pp. 4015–4022, May 2018.
- [35] H. Liu, X. Xie, X. Gao, H. Liu, and Y. Li, "Stability analysis of SSR in multiple wind farms connected to series-compensated systems using impedance network model," *IEEE Trans. Power Syst.*, vol. 33, no. 3, pp. 3118–3128, May 2018.
- [36] H. Liu, X. Xie, and W. Liu, "An oscillatory stability criterion based on the unified dq -frame impedance network model for power systems with high-penetration renewables," *IEEE Trans. Power Syst.*, vol. 33, no. 3, pp. 3472–3485, May 2018.
- [37] C. Yoon, H. Bai, X. Wang, C. L. Bak, and F. Blaabjerg, "Regional modeling approach for analyzing harmonic stability in radial power electronics based power system," in *Proc. IEEE 2015 6th International Symposium on Power Electronics for Distributed Generation Systems (PEDG)*, pp. 1–5.
- [38] W. Cao, X. Zhang, Y. Ma, and F. Wang, "Stability criterion and controller parameter design of radial-line renewable systems with multiple inverters," in *Proc. IEEE 2016 Applied Power Electronics Conference and Exposition (APEC)*, pp. 2229–2236.
- [39] W. Zhou, Y. Wang, and Z. Chen, "Decoupled multi-port impedance modelling method of transmission network in inverter-fed power plant," in *Proc. IEEE 2018 International Conference on Smart Grid (icSmartGrid)*, pp. 129–135.
- [40] L. Harnefors, L. Zhang, and M. Bongiorno, "Frequency-domain passivity-based current controller design," *IET Power Electron.*, vol. 1, no. 4, pp. 455–465, Dec. 2008.
- [41] L. Harnefors, A. G. Yepes, A. Vidal, and J. Doval-Gandoy, "Passivity-based controller design of grid-connected VSCs for prevention of electrical resonance instability," *IEEE Trans. Ind. Electron.*, vol. 62, no. 2, pp. 702–710, Feb. 2015.
- [42] J. Khazaei, M. Beza, and M. Bongiorno, "Impedance analysis of modular multi-level converters connected to weak AC grids," *IEEE Trans. Power Syst.*, vol. 33, no. 4, pp. 4015–4025, Jul. 2018.
- [43] M. Amin and M. Molinas, "Small-signal stability assessment of power electronics based power systems: A discussion of impedance-and eigenvalue-based methods," *IEEE Trans. Ind. Appl.*, vol. 53, no. 5, pp. 5014–5030, Sep./Oct. 2017.
- [44] M. K. Bakhshizadeh, F. Blaabjerg, J. Hjerrild, Ł. Kocewiak, and C. L. Bak, "Improving the impedance-based stability criterion by using the vector fitting method," *IEEE Trans. Energ. Convers.*, vol. 33, no. 4, pp. 1739–1747, Dec. 2018.
- [45] B. Gustavsen and A. Semlyen, "Rational approximation of frequency domain responses by vector fitting," *IEEE Trans. Power Del.*, vol. 14, no. 3, pp. 1052–1061, Jul. 1999.
- [46] B. Gustavsen, "Improving the pole relocating properties of vector fitting," *IEEE Trans. Power Del.*, vol. 21, no. 3, pp. 1587–1592, Jul. 2006.
- [47] A. Rygg and M. Molinas, "Apparent impedance analysis: A small-signal method for stability analysis of power electronic-based systems," *IEEE J. Emerg. Sel. Top. Power Electron.*, vol. 5, no. 4, pp. 1474–1486, Dec. 2017.
- [48] M. K. Bakhshizadeh, C. Yoon, J. Hjerrild, C. L. Bak, Ł. H. Kocewiak, F. Blaabjerg, and B. Hesselbæk, "The application of vector fitting to eigenvalue-based harmonic stability analysis," *IEEE J. Emerg. Sel. Top. Power Electron.*, vol. 5, no. 4, pp. 1487–1498, Dec. 2017.
- [49] W. Dong, H. Xin, D. Wu, and L. Huang, "Small signal stability analysis of multi-infeed power electronic systems based on grid strength assessment," *IEEE Trans. Power Syst.*, vol. 34, no. 2, pp. 1393–1403, Mar. 2019.
- [50] F. Liu, J. Liu, H. Zhang, and D. Xue, "Stability issues of Z+ Z type cascade system in hybrid energy storage system (HESS)," *IEEE Trans. Power Electron.*, vol. 29, no. 11, pp. 5846–5859, Nov. 2014.
- [51] B. Moore, "Principal component analysis in linear systems: Controllability, observability, and model reduction," *IEEE Trans. Autom. Control*, vol. 26, no. 1, pp. 17–32, Feb. 1981.
- [52] M. Tarokh, "Frequency-domain criteria for controllability and observability of multivariable systems," in *Proc. IEEE 1986 American Control Conference*, pp. 782–787.
- [53] Y. Hu, W. Wu, A. M. Gole, and B. Zhang, "A guaranteed and efficient method to enforce passivity of frequency-dependent network equivalents," *IEEE Trans. Power Syst.*, vol. 32, no. 3, pp. 2455–2463, May 2017.
- [54] D. Yang, X. Ruan, and H. Wu, "Impedance shaping of the grid-connected inverter with LCL filter to improve its adaptability to the weak grid condition," *IEEE Trans. Power Electron.*, vol. 29, no. 11, pp. 5795–5805, Nov. 2014.
- [55] W. Zhou, Y. Wang, and Z. Chen, "A gray-box parameters identification method of voltage source converter using vector fitting algorithm," in *Proc. IEEE 2019 10th International Conference on Power Electronics and ECCE Asia (ICPE 2019-ECCE Asia)*, pp. 2948–2955.
- [56] M. Beza and M. Bongiorno, "On the risk for subsynchronous control interaction in type 4 based wind farms," *IEEE Trans. Sustain. Energy*, vol. 10, no. 3, pp. 1410–1418, Jul. 2019.
- [57] A. Rygg, M. Molinas, C. Zhang, and X. Cai, "On the equivalence and impact on stability of impedance modeling of power electronic converters in different domains," *IEEE J. Emerg. Sel. Top. Power Electron.*, vol. 5, no. 4, pp. 1444–1454, Dec. 2017.



Weihua Zhou (S'18) was born in Anhui, China, in 1993. He received the B.Eng. degree in electrical engineering from Honors College, Northwestern Polytechnical University, Xi'an, China, and the M.Sc. degree in electrical engineering at the same university, in 2014 and 2017, respectively. He is currently working toward the Ph.D. degree in electrical engineering with the Department of Energy Technology, Aalborg University, Aalborg, Denmark.

From November 2015 to May 2016, he was a Junior Research Assistant at the Department of Mechanical and Automation Engineering, The Chinese University of Hong Kong, Hong Kong. His research interests include modeling and control of grid-connected converters, and small-signal stability analysis of power electronic-dominated power systems.

Mr. Zhou was the recipient of the Best Paper Award in 6th International Conference on Smart Grids (icSmartGrid) cosponsored by IEEE Industry Application Society in 2018.



Raymundo E. Torres-Olguin received the B.Sc. degree in electromechanical engineering from the University of San Luis Potosí, Mexico, in 2004, M.Sc. degree in control and dynamical systems from the Applied Mathematics Department, Research Institute of Science and Technology of San Luis Potosí (IPICYT), Mexico, in 2006, and Ph.D. degree in electric power engineering from the Norwegian University of Science and Technology (NTNU), Norway, in 2013.

From 2012, he has worked as a research scientist in SINTEF Energy Research located in Trondheim, Norway. His main research interest includes control of power electronics for the integration of renewable resources, dc transmission, and microgrids.



Yanbo Wang (S'15-M'17-SM'19) received the Ph.D. degree in electrical engineering at the Department of Energy Technology, Aalborg University, Aalborg, Denmark, in 2017. Currently, he is with the Department of Energy Technology in Aalborg University as an Assistant Professor.

From June to October of 2016, he was a visiting scholar in Power System Research Group of the Department of Electrical and Computer Engineering, University of Manitoba, Winnipeg, MB, Canada. His research interests include distributed power generation system, wind power system, microgrid, as well as operation and control technologies of power electronic-dominated power system.

Dr. Wang's paper on Distributed Power System received the First Prize Paper Award of the 6th International Conference of Smart Grid cosponsored by IEEE Industry Application Society in 2018. He received the Best Session Paper Award at the annual conference of the IEEE Industrial Electronics Society in 2015 in Japan.



Zhe Chen (M'95-SM'98-F'19) received the B.Eng. and M.Sc. degrees all in electrical engineering from Northeast China Institute of Electric Power Engineering, Jilin City, China, MPhil in power electronic from Staffordshire University, England and the Ph.D. degree in electrical engineering from University of Durham, England.

Dr. Chen is a full Professor with the Department of Energy Technology, Aalborg University, Aalborg, Denmark. He is the leader of Wind Power System Research program at the Department of Energy Technology, Aalborg University and the Danish Principle Investigator for Wind Energy of Sino-Danish Centre for Education and Research. His research areas are power systems, power electronics and electric machines, and his main current research interests are wind energy and modern power systems. He has led many research projects and has more than 500 publications in his technical fields.